nature structural & molecular biology

ARTICLES

https://doi.org/10.1038/s41594-020-0399-3

Check for updates

Hsp27 chaperones FUS phase separation under the modulation of stress-induced phosphorylation

Zhenying Liu[1,2,6], Shengnan Zhang[1,2,6], Jinge Gu[1,2,6], Yilun Tong[1,2], Yichen Li[3], Xinrui Gui[1,2], Houfang Long[1,2], Chuchu Wang[1,2], Chunyu Zhao[1,2], Jinxia Lu[3], Lin He[3], Ying Li[1,2], Zhijun Liu[4], Dan Li[3,5]✉ and Cong Liu[1,2]✉

Protein phase separation drives the assembly of membraneless organelles, but little is known about how these membraneless organelles are maintained in a metastable liquid- or gel-like phase rather than proceeding to solid aggregation. Here, we find that human small heat-shock protein 27 (Hsp27), a canonical chaperone that localizes to stress granules (SGs), prevents FUS from undergoing liquid–liquid phase separation (LLPS) via weak interactions with the FUS low complexity (LC) domain. Remarkably, stress-induced phosphorylation of Hsp27 alters its activity, leading Hsp27 to partition with FUS LC to preserve the liquid phase against amyloid fibril formation. NMR spectroscopy demonstrates that Hsp27 uses distinct structural mechanisms for both functions. Our work reveals a fine-tuned regulation of Hsp27 for chaperoning FUS into either a polydispersed state or a LLPS state and suggests an essential role for Hsp27 in stabilizing the dynamic phase of stress granules.

Numerous RNA-binding proteins can undergo LLPS, which drives the formation of membraneless organelles, such as SGs and P-granules, in response to different cellular stress and stimuli[1–3]. Many RNA-binding proteins, for example, FUS, hnRNPA1 and TDP43, possess a high intrinsic propensity to self-assemble[4–6]. They can spontaneously undergo LLPS and further condense into amyloid fibrils in vitro or in disease models[5,7,8]. While in normal cells the self-organization of these proteins is strictly controlled and maintained in a dynamic liquid- or gel-like state, dysregulation leads to pathological amyloid aggregation and neurodegenerative diseases, for example, amyotrophic lateral sclerosis (ALS)[8,9]. However, it is unclear how the metastable state of the membraneless organelles is maintained in vivo.

Molecular chaperones are vital in maintaining protein homeostasis and preventing protein misfolding and aggregation[10,11]. The dynamic assembly of SGs is also under the regulation of chaperones[9]. Recent studies have shown that nuclear-import receptors can serve as molecular chaperones to prevent FUS phase separation[12–15]. There are actually many canonical chaperones that have been identified in SGs, including Hsp27, Hsp40, Hsp60 and Hsp90[16,17]. In particular, Hsp27 has been reported to be closely associated with ALS[18,19]. Genetic mutation in the Hsp27 promoter (*HSPB1*) has been identified in sporadic ALS, which impairs the Hsp27 stress response[20]. Hsp27 is significantly upregulated in patients with familial and sporadic ALS[19]. Mutation of Hsp27 can directly lead to hereditary motor neuron diseases (for example, distal hereditary motor neuropathy and Charcot-Marie-Tooth disease type 2)[21].

Hsp27, also known as HSPB1, is a ubiquitous small heat-shock protein widely expressed in cells including the cytosol and nucleus[22,23]. It plays an important role in protein homeostasis, especially under stress conditions[24]. It is composed of a hydrophobic N-terminal domain (NTD), a highly conserved α-crystallin domain (ACD) and a flexible C-terminal domain (CTD)[25]. Hsp27 presents as an ensemble of high-order multimers (~500–1,100 kDa) in aqueous solution[24,26]. Previous studies have shown that Hsp27 exhibits potent chaperone activity in preventing proteins, such as α-synuclein, Tau and SOD1, from both amorphous and amyloid aggregation[25,27–29]. In response to stress, Hsp27 is phosphorylated at S15, S78 and S82 of the NTD, which leads to enhanced activity of Hsp27 against amorphous aggregation[30]. In this study, we describe the chaperone activity of Hsp27 in FUS phase separation. We find that the activity of Hsp27 is switched by phosphorylation between inhibition of FUS LLPS and amyloid aggregation. Furthermore, we show that the two activities are based on distinct molecular mechanisms. This work illuminates the essential role of chaperones in the maintenance of the dynamics of SGs in cells.

Results

Hsp27 inhibits the SG association of FUS. To investigate the biological impact of Hsp27 on the SG association of FUS, we first probed the endogenous Hsp27 in HeLa cells with Hsp27 antibody and observed that upon stress, Hsp27 condensed in the SGs (Extended Data Fig. 1a). In cells overexpressing FUS, Hsp27 colocalized with FUS in SGs (Extended Data Fig. 1b). Next, we knocked out Hsp27 in HeLa cells (Hsp27 KO) (Extended Data Fig. 2a,b). In the KO cells, we found a significantly increased amount of FUS protein entering the SGs (Fig. 1a), with similar expression levels of FUS in the KO and wild-type cells (Extended Data Fig. 2c). Notably, FUS aggregation was also observed in the Hsp27-KO cells, but not in the wild-type cells (Fig. 1a).

Consistent with the Hsp27-KO result, overexpression of Hsp27 in HeLa cells showed significantly less FUS protein being recruited

[1]Interdisciplinary Research Center on Biology and Chemistry, Shanghai Institute of Organic Chemistry, Chinese Academy of Sciences, Shanghai, China. [2]University of the Chinese Academy of Sciences, Shijingshan District, Beijing, China. [3]Bio-X Institutes, Key Laboratory for the Genetics of Developmental and Neuropsychiatric Disorders, Ministry of Education, Shanghai Jiao Tong University, Shanghai, China. [4]National Facility for Protein Science in Shanghai, Zhangjiang Lab, Shanghai Advanced Research Institute, Chinese Academy of Sciences, Shanghai, China. [5]Bio-X-Renji Hospital Research Center, Renji Hospital, School of Medicine, Shanghai Jiao Tong University, Shanghai, China. [6]These authors contributed equally: Zhenying Liu, Shengnan Zhang, Jinge Gu. ✉e-mail: lidan2017@sjtu.edu.cn; liulab@sioc.ac.cn

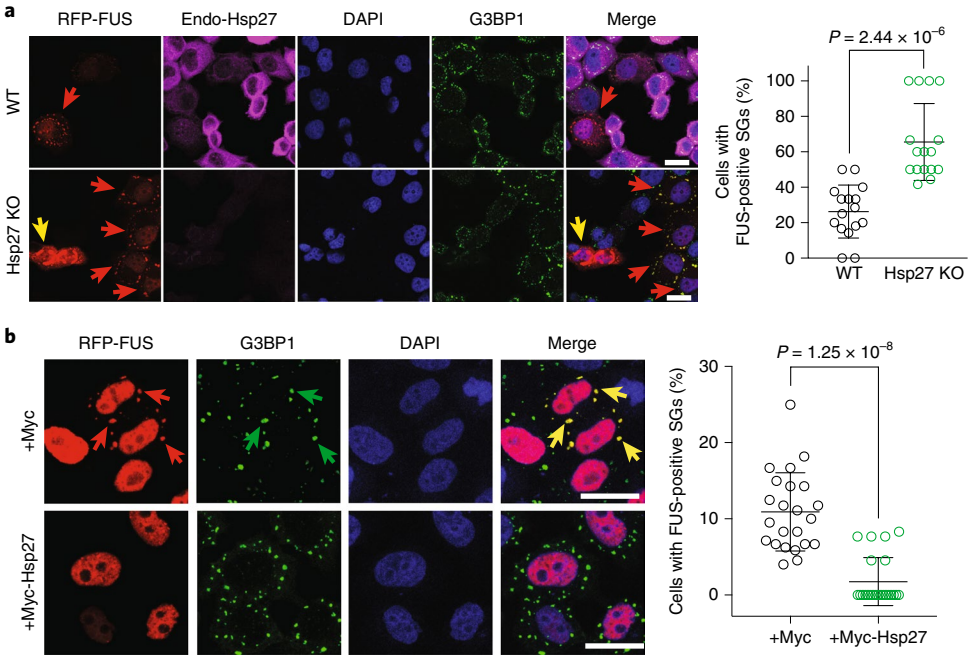

Fig. 1 | Hsp27 inhibits FUS from associating with SGs. a, SG association of FUS in wild-type (WT) and Hsp27-KO HeLa cells. Cells transfected with RFP-tagged FUS (red) and stressed by the addition of 0.5 mM sodium arsenite were immunostained for endogenous Hsp27 (Endo-Hsp27, purple), DAPI (blue) and G3BP1 (SG marker, green). Red arrows indicate cells with FUS-positive SGs. Yellow arrows indicate FUS aggregation. Scale bars, 20 μm. Right, statistics of FUS-positive SGs in 225 FUS-overexpressed cells from 32 images of four biologically independent samples. *P* value based on two-sided Student's *t* test. **b**, SG association of FUS upon Hsp27 overexpression. HeLa cells were transfected with RFP-FUS and Myc-Hsp27 (or Myc as a control) and stressed with 0.5 mM sodium arsenite. Arrows indicate SGs. Scale bars, 20 μm. Right, statistics of FUS-positive SGs in 740 FUS-overexpressing cells from 46 images of five biologically independent samples. *P* value based on two-sided Student's *t* test. Source data for graphs in **a**,**b** are available online.

into SGs (Fig. 1b). Western blot confirmed the overexpression of transfected Hsp27 (Extended Data Fig. 2d), and the overexpression of Hsp27 did not influence the levels of other small heat-shock proteins, such as αB crystallin (αBc; Extended Data Fig. 2e). The expression level of FUS also did not change upon Hsp27 overexpression (Extended Data Fig. 2f). Additionally, western blot showed that stress stimulated the expression of endogenous Hsp27 (Extended Data Fig. 2d). Together, these results suggest that Hsp27 is active in inhibiting FUS LLPS and its association with SGs.

Hsp27 acts on FUS LC, rather than the RGG-rich domain. FUS contains multiple intrinsically disordered regions, including an N-terminal LC domain and a C-terminal RGG-rich domain (FUS RGG; Fig. 2a), which drive LLPS of full-length FUS. To identify which intrinsically disordered region of FUS is the client of Hsp27, we investigated the activity of Hsp27 on FUS LC (residues 1–163) and FUS RGG (residues 371–526) (Fig. 2a). We first induced the LLPS of FUS LC by decreasing the temperature from 25 °C to 4 °C[31]. As the temperature decreased, the FUS LC solution became cloudy (Fig. 2b), and liquid-like droplets were observed via differential interference contrast (DIC) and fluorescence microscopy (Fig. 2b). In contrast with this, in the presence of Hsp27 at substoichiometric molar ratios, the FUS LC solution remained clear as the temperature decreased, and no obvious liquid-like droplets formed (Fig. 2b). The turbidity of the solution at a wavelength of 600 nm quantitatively showed a concentration-dependent inhibition of Hsp27 to the LLPS of FUS LC (Fig. 2c). Furthermore, we observed that as Hsp27 was added to the preformed droplets of FUS LC, a significant number of droplets dissembled (Extended Data Fig. 3a), and the turbidity of the solution decreased accordingly (Extended Data Fig. 3b). We examined another small heat-shock protein, αBc (also known as HSPB5), which has an overall 45% sequence identity with Hsp27 and a similar structural organization (refs. [32,33]) (Extended Data Fig. 4), and it showed no activity on the LLPS of FUS LC (Extended Data Fig. 3a,c).

We then tested the activity of Hsp27 on FUS RGG. The LLPS of FUS RGG was also induced by decreasing the temperature to 4 °C. At substoichiometric molar ratios, Hsp27 showed no activity on the LLPS of FUS RGG, whereas as the molar ratio increased to 1:3 (FUS RGG:Hsp27), a slight inhibition was observed, with no statistical significance (Extended Data Fig. 3d,e). Thus, our results indicate that the inhibition of Hsp27 on FUS LLPS is mainly through the inhibition of LLPS of FUS LC rather than of the RGG-rich domain.

Hsp27 binds to FUS LC via weak interactions. We then utilized NMR spectroscopy to study the structural mechanism underlying the interaction between Hsp27 and FUS LC. The ^{1}H-^{15}N HSQC spectrum of ^{15}N-labeled FUS LC (50 μM, pH 7.0, 25 °C) showed that FUS LC adopted an intrinsically disordered conformation with a narrow chemical shift dispersion in the ^{1}H dimension (backbone amide resonances within 7.8–8.8 ppm) (Extended Data Fig. 5a), which is similar to results in previous studies[34]. As we titrated Hsp27 to FUS LC, the HSQC spectrum of FUS LC showed a global decrease of signal intensities in a concentration-dependent manner (Fig. 2d and Extended Data Fig. 5b). FUS LC residues generally showed a ~40% decrease in intensity upon equimolar Hsp27 titration (Fig. 2d). As a control, we titrated FUS LC with bovine serum albumin (BSA). The result showed that BSA exhibits no significant perturbation on the signal intensities of FUS LC (Extended Data Fig. 5c). FUS LC is composed of limited types of amino acids including alanine, glycine, asparagine, glutamine, serine, threonine, tyrosine and aspartate. Small chemical shift perturbations upon titration were observed on serine residues but not the others (Fig. 2e). Consist

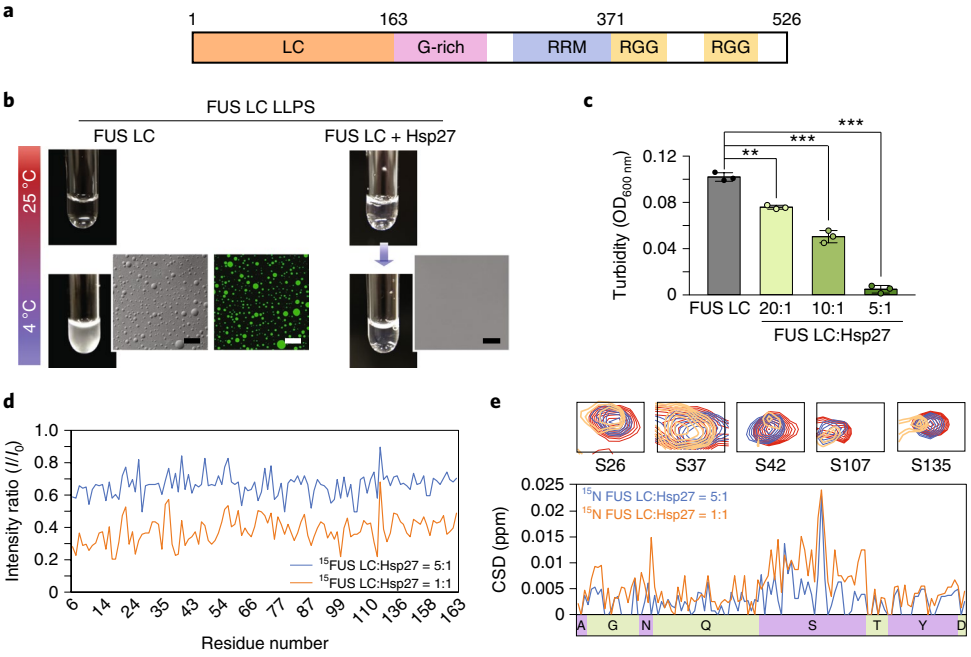

Fig. 2 | Hsp27 inhibits FUS LC LLPS via weak interactions. a, Domain organization of FUS. **b**, Effect of Hsp27 on LLPS of FUS LC. Test tubes contain 150 μM FUS LC in the absence or presence of 30 μM Hsp27. DIC and fluorescence images are shown. Scale bars, 10 μm. **c**, Turbidity measurement of 150 μM FUS LC in the presence of indicated ratios of Hsp27 at 4 °C. Graphs correspond to mean ± s.d., with $n = 3$ biologically independent samples. $^{**}P < 0.01$; $^{***}P < 0.001$. *P* values based on two-sided Student's *t* test. **d**, Residue-specific intensity changes of signals in the 2D ^{1}H-^{15}N HSQC spectra of 50 μM ^{15}N-labeled FUS LC in the presence of Hsp27 at molar ratios (FUS LC:Hsp27) of 5:1 (blue) and 1:1 (orange). **e**, Top, spectra of resonances with relatively large chemical shift perturbations. Bottom, residue-specific chemical shift deviations (CSD). The *x* axis is based on the amino acid composition of FUS LC. Source data for **c** are available online.

with this finding, when we mutated the serine residues to alanine, we found that the mutations significantly impaired the inhibition activity of Hsp27 on the LLPS of FUS LC (Extended Data Fig. 6). Taken together, these results indicate that Hsp27 binds FUS LC via transient weak interactions to a wide region across the FUS LC, with a slight preference for serine residues.

Hsp27 interferes with long-range intra- and intermolecular transient interactions of FUS LC. To investigate how Hsp27 influences the self-assembly of FUS LC, we conducted an NMR paramagnetic relaxation enhancement (PRE) experiment that can characterize the transient and long-range (spatial distance: 15–24 Å) interactions inside or between FUS LC molecules. Covalent attachment of a paramagnetic nitroxide spin label to a cysteine enhances the transverse relaxation rate of protons that are proximal to the spin label (<24 Å), which results in a decrease in the NMR signal intensities of these protons. This effect is eliminated once the spin label is reduced (diamagnetic). The PRE effect can be quantified using the NMR signal intensity ratio (I_{param}/I_{diam}) of each residue from the two dimensional (2D) ^{1}H-^{15}N HSQC spectra at the paramagnetic and diamagnetic states, as previously reported[35,36]. Normally, an intensity ratio of >0.95 indicates a distance exceeding 25 Å[37]. Here, methanethiosulfonate (MTSL) was used as a paramagnetic spin label and was first introduced into FUS LC at residue A16 through an A16C mutation and conjugation (Fig. 3a). We collected the HSQC spectra of the MTSL-labeled ^{15}N-FUS LC (paramagnetic) after reduction of the nitroxide radical (diamagnetic). Intriguingly, the I_{param}/I_{diam} profile of A16C-MTSL-labeled FUS LC revealed that a wide range of residues are involved in the long-distance interactions with A16C MTSL (Fig. 3a). Alternatively, we introduced MTSL into the middle (S70) and C-terminal (S127) sites of FUS LC. The I_{param}/I_{diam} of the MTSL-labeled S70C and S127C ^{15}N-FUS LC showed a similar global decrease across the FUS LC (Extended Data Fig. 7), further confirming extensive long-range and transient contacts within and/or between FUS LC molecules.

We next sought to specifically probe the intermolecular interactions between FUS LC molecules. We mixed A16C-MTSL-labled, but not ^{15}N-labeled, FUS LC with ^{15}N-labeled, but not A16C-MTSL-labeled, FUS LC at a molar ratio of 1:1. The I_{param}/I_{diam} of the mixture showed a significant decrease, especially in the regions of residues 13–45, 50–78, 90–130 and 155–160 (Fig. 3b). Because the ^{15}N-labeled FUS LC was not labeled with MTSL, the decrease of I_{param}/I_{diam} could only come from intermolecular interactions between FUS LC molecules. Consistent with this notion, as we added unlabeled FUS LC into ^{15}N-A16C-MTSL-labeled FUS LC, the I_{param}/I_{diam} revealed a slight but concentration-dependent increase of the attenuated intensities, which is likely to be caused by disruption of the intermolecular contacts between FUS LC molecules (Fig. 3b).

Furthermore, we added Hsp27 into the ^{15}N-A16C-MTSL-labeled FUS LC. We observed that the drop of the I_{param}/I_{diam} was also restored, similar to that seen with the addition of unlabeled FUS LC (Fig. 3c). The same results were obtained with MTSL labeling on the S70 and S127 sites (Extended Data Fig. 7). As a control, BSA, which does not interact with FUS LC, exhibited no effect on the intensity of FUS LC (Extended Data Fig. 7c). Taken together, the PRE data suggest that FUS LC molecules form extensive, transient, long-range intra- and intermolecular interactions in solution, rendering the occurrence of LLPS, whereas, the binding of Hsp27 can diminish the self-association of FUS LC molecules and thus block their assembly into liquid-like droplets (Fig. 3d).

The NTD and multimerization of Hsp27 are essential for its inhibitory activity on LLPS. We next sought to dissect the role of each Hsp27 domain in the binding of FUS. Hsp27 contains a central ACD flanked by an NTD and CTD (Fig. 4a). We first examined whether the ACD is as active in inhibiting the LLPS of FUS LC as the

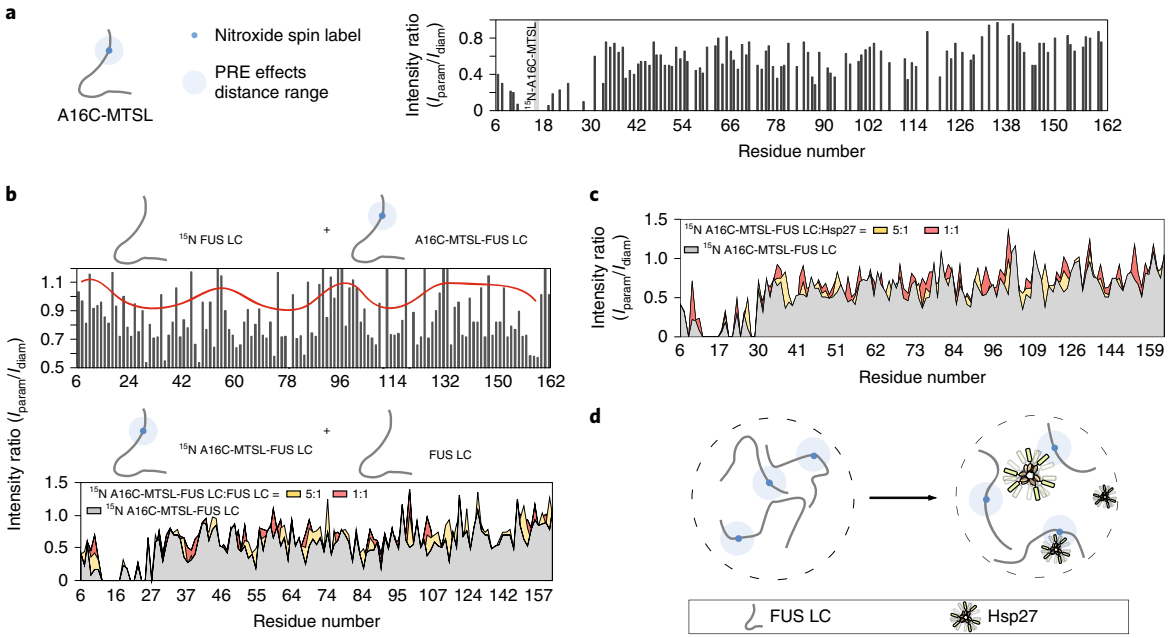

Fig. 3 | Effect of Hsp27 on the long-range and transient interactions in FUS LC probed by paramagnetic relaxation enhancement. a, The PRE profile of 50 μM ^{15}N-labeled A16C-MTSL-FUS LC. A16 of FUS LC was mutated to cysteine, and a nitroxide spin label (MTSL) was attached. **b**, The PRE profile of 50 μM ^{15}N-labeled FUS LC in the presence of 50 μM A16C-MTSL-FUS LC is shown on top. The red line indicates the regions that undergo intermolecular PRE effects. The PRE profile of 50 μM ^{15}N-labeled A16C-MTSL-FUS LC in the presence of FUS LC is shown on the bottom. The PRE attenuations were gradually recovered with increasing concentrations of FUS LC: 10 μM (yellow) and 50 μM (red). **c**, The PRE profile of 50 μM ^{15}N-labeled A16C-MTSL-FUS LC in the presence of 10 μM (yellow) or 50 μM Hsp27 (red). **d**, A schematic diagram showing that the long-range and transient interactions of FUS LC are weakened by Hsp27.

full-length Hsp27, as the ACD has been reported as the major active domain for the chaperone activity of Hsp27 (refs. [25,38]). Intriguingly, we found that the ACD alone nearly completely lost inhibitory activity on LLPS (Fig. 4b). We then extended the ACD by including either the NTD (ΔCTD) or the CTD (ΔNTD). The result showed that ΔNTD is still inactive in inhibiting FUS LC LLPS (Fig. 4b). In contrast, ΔCTD delayed the initiation of LLPS, in particular at ~12 °C and below (Fig. 4b). At 12 °C, ΔCTD effectively inhibited droplet formation of FUS LC (Fig. 4c). These results indicate that the Hsp27 NTD, but not other regions, is essential for the inhibitory activity of Hsp27 on FUS LC LLPS.

We noticed that the activity of ΔCTD was weaker than that of the full-length Hsp27 (Figs. 2c and 4b), which suggests that the CTD may also play a role in LLPS inhibition. Full-length Hsp27 presents as highly polydispersed multimers with molecular weights ranging from 500 to 1,100 kDa[24,26] (Fig. 4d). The CTD is known to be important for the multimerization of Hsp27 (refs. [24,39]). Indeed, the result of analytical ultracentrifugation showed that truncation of the CTD largely disrupted the multimerization of Hsp27 (Fig. 4d). Thus, we asked whether the weakened activity of ΔCTD was due to the deficiency in multimerization. To test this assumption, we replaced the NTD of αBc with that of Hsp27 (named N_{Hsp27}-αBc) (Fig. 4e). The result showed that N_{Hsp27}-αBc formed high-order multimers, which were efficient in inhibiting LLPS of FUS LC (Fig. 4f,g and Extended Data Fig. 8a). Conversely, when we replaced the NTD of Hsp27 with that of αBc (named $N_{αBc}$-Hsp27), the chimeric protein was inactive, although it could form multimers (Fig. 4f,g and Extended Data Fig. 8a). Taken together, our data indicate that the NTD is essential for the inhibitory activity of Hsp27 on FUS LC LLPS, which is further boosted by multimerization of Hsp27.

Stress-induced phosphorylation of Hsp27 weakens its inhibitory activity on LLPS. It is known that under stress conditions, Hsp27 is phosphorylated at residues S15, S78 and S82 of the NTD[30,40]. Because the NTD is necessary for the activity of Hsp27 in FUS LLPS, we examined whether the stress-induced phosphorylation influences this activity. We mutated the three serine residues to aspartate to mimic phosphorylated Hsp27 (Fig. 5a). Notably, the resulted mutant, named Hsp27-3D, exhibited significantly weakened activity in inhibiting FUS LC LLPS compared with that of the wild type (Fig. 5b,c). We found that the molecular weight of Hsp27-3D decreased to ~50 kDa (Fig. 5d), which indicates that the phosphorylation may obstruct the full assembly of multimers. Additionally, we examined the influence of the 3D mutation on the activity of ΔCTD. The result showed that the 3D mutations abolished the moderate activity of ΔCTD (Extended Data Fig. 8b). Thus, our data indicate that stress-induced phosphorylation may diminish the interaction between the Hsp27 NTD and the FUS LC, as well as the multimeric assembly of Hsp27, which weakens the inhibitory activity of Hsp27 in the LLPS of FUS LC.

Hsp27-3D phase separates with FUS LC to chaperone its LLPS state against amyloid aggregation. As phosphorylation weakened the inhibitory activity of Hsp27 on LLPS, FUS LC spontaneously underwent LLPS in the presence of Hsp27-3D (Fig. 5b,c). Intriguingly, we found that Hsp27-3D efficiently entered the droplets of FUS LC, and thus phase separated with FUS LC (Fig. 5e). More importantly, Hsp27-3D preserved the liquid-like property of FUS LC droplets within a significant period of time (more than 20 h) (Fig. 5f). In contrast, in the absence of Hsp27-3D, amyloid fibrils remarkably grew out from the droplets of FUS LC within the same period of time (Fig. 5f). Fluorescence recovery after photobleaching (FRAP) further showed that in the presence of Hsp27-3D, the diffusion of FUS LC molecules was faster than that in the absence of Hsp27-3D, which indicates that Hsp27-3D prevents the hardening and maturation of FUS LC droplets (Fig. 5g).

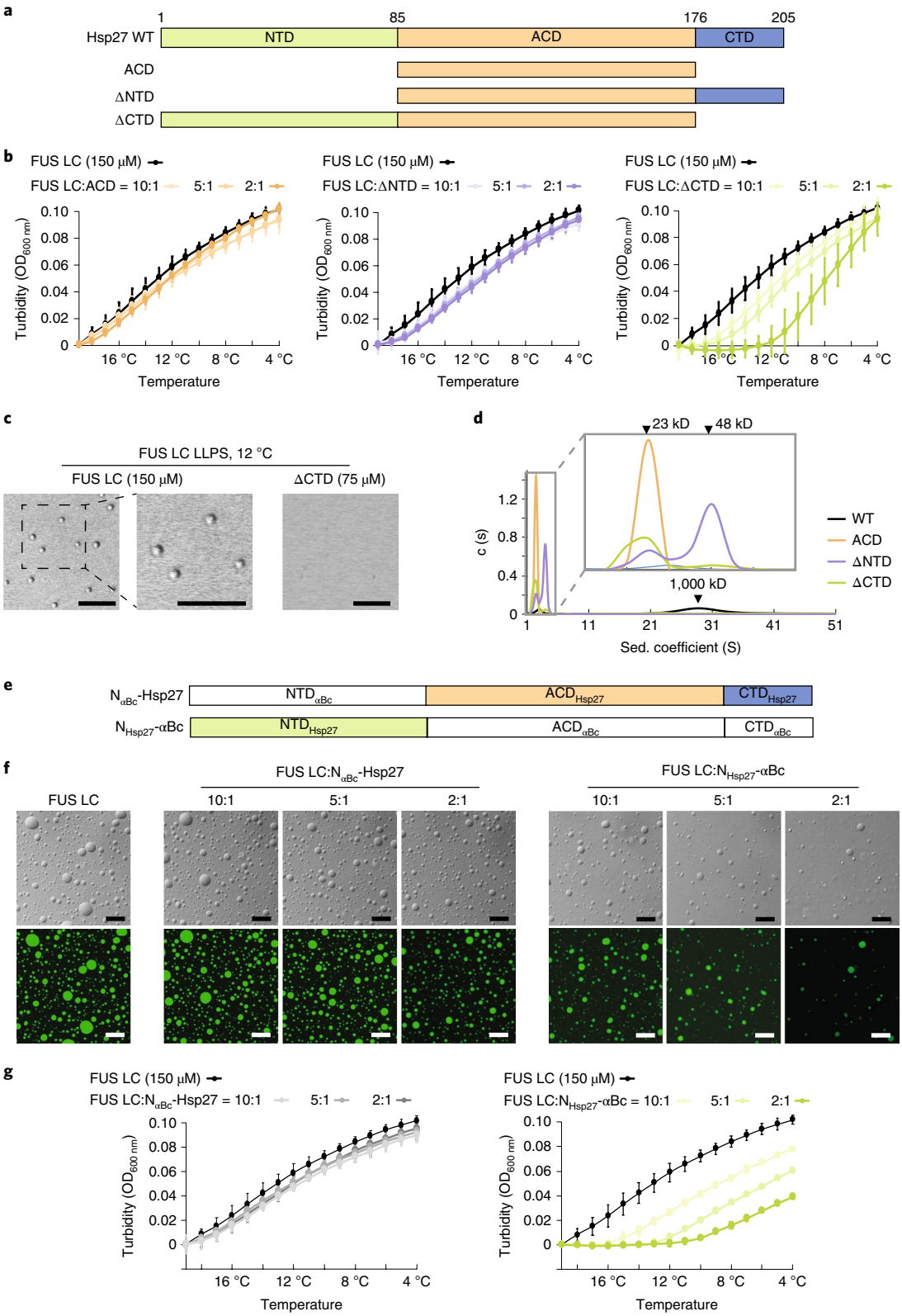

Fig. 4 | Characterization of Hsp27 domains that account for LLPS inhibition. a, Domain organization of Hsp27 and recombinant variants. **b**, Influences of Hsp27 variants on the phase diagram of FUS LC. The turbidity of 150 μM FUS LC in the presence of indicated concentrations of Hsp27 variants was measured at $OD_{600\,nm}$ as the temperature decreased from 19 °C to 4 °C. Data are plotted as mean ± s.d., with $n = 3$ biologically independent samples. **c**, DIC images of FUS LC in the absence and presence of Hsp27 ΔCTD, respectively, at 12 °C. Scale bar, 10 μm. **d**, Sedimentation velocity analysis of Hsp27 variants. A zoomed-in view of sedimentation coefficient at 1–6 s is shown. Molecular weights are indicated. **e**, Domain organizations of $N_{αBc}$-Hsp27 and N_{Hsp27}-αBc. **f**, DIC and fluorescence images of 150 μM FUS LC in the absence and presence of $N_{αBc}$-Hsp27 and N_{Hsp27}-αBc at the indicated concentrations. Scale bar, 10 μm. **g**, Turbidity (measured at $OD_{600\,nm}$) of 150 μM FUS LC in the absence and presence of $N_{αBc}$-Hsp27 (left) and N_{Hsp27}-αBc (right) at the indicated concentrations. Data are plotted as mean ± s.d., with $n = 3$ biologically independent samples. Source data for graphs in **b**,**g** are available online.

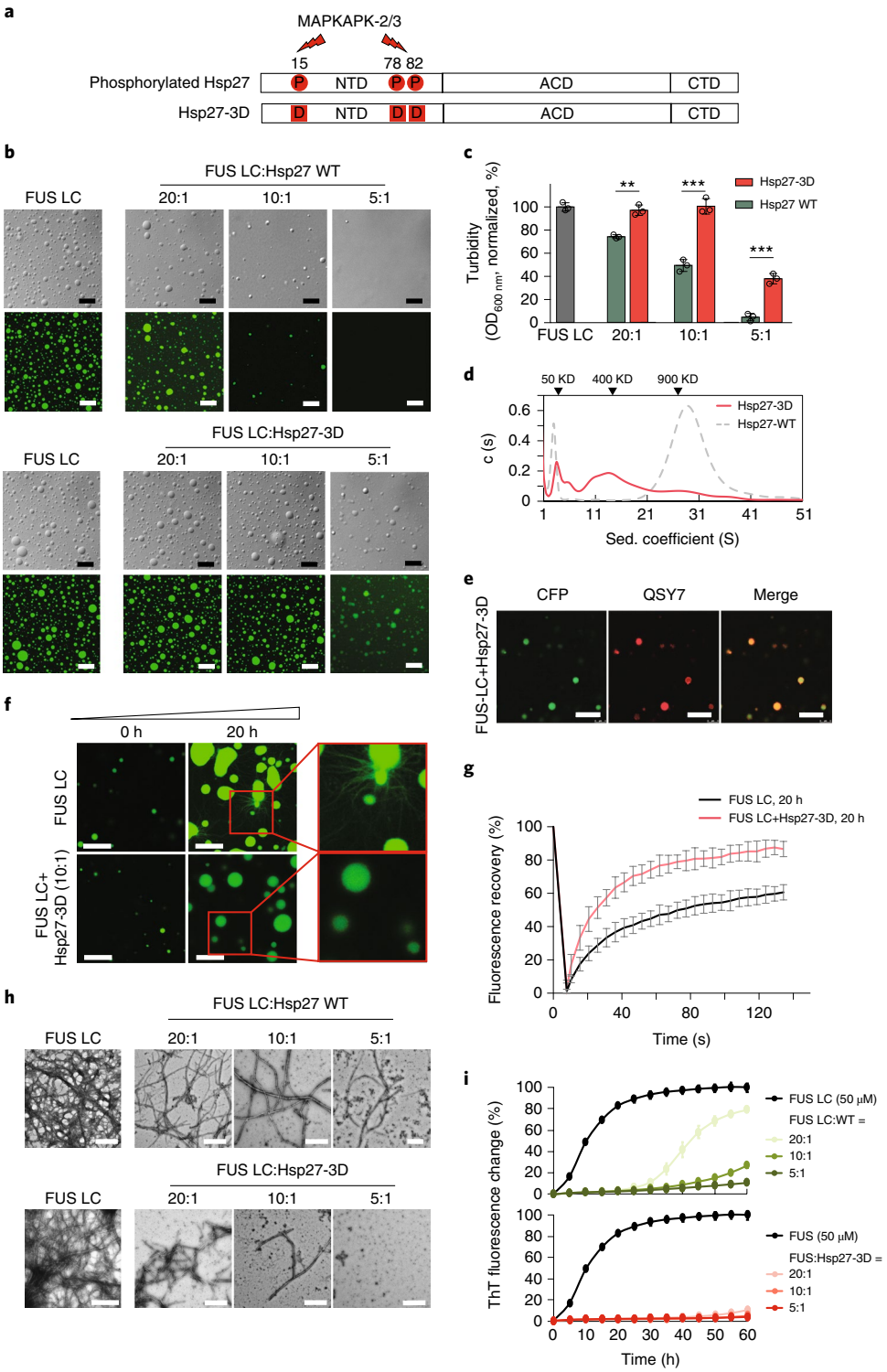

Fig. 5 | Hsp27-3D phase separates with FUS LC and inhibits amyloid fibril formation. a, Stress-induced phosphorylation sites of Hsp27 and the phosphomimetic construct Hsp27-3D. **b**, DIC and fluorescence images of FUS LC (150 μM) in the absence and presence of Hsp27 WT (top) and Hsp27-3D (bottom) at the indicated concentrations. Scale bar, 10 μm. **c**, Normalized turbidities ($OD_{600\,nm}$) of FUS LC in the presence of Hsp27-WT and Hsp27-3D. Data are plotted as mean ± s.d., with $n = 3$ biologically independent samples. $^{**}P < 0.01$ and $^{***}P < 0.001$. *P* values based on two-sided Student's *t* test. **d**, Sedimentation velocity analysis of Hsp27 WT (14 μM) and Hsp27-3D (13 μM). Molecular weights are indicated. **e**, Confocal microscopic images of 100 μM FUS LC with 100 μM Hsp27-3D. FUS LC is labeled with CFP; Hsp27 is labeled with QSY7. Scale bar, 10 μm. **f**, Fluorescence images of FUS LC (100 μM) droplets in the absence or presence of Hsp27-3D at a ratio of 10:1 at 0 and 20 h. Scale bars, 10 μm. **g**, Recovery of FUS LC droplets examined via FRAP assay. The time point right after photobleaching is set to 0. Data shown are means ± s.d., with $n = 3$ individual droplets. **h**, Transmission electron microscopy images of FUS LC (50 μM) alone and in the presence of Hsp27 WT or Hsp27-3D at indicated molar ratios. Scale bars, 500 nm. **i**, ThT fluorescence profiles of FUS LC (with 0.5% seeds) in the absence and presence of Hsp27 WT and Hsp27-3D at the indicated concentrations. Data are plotted as mean ± s.d., with $n = 3$ biologically independent samples. Source data for graphs in **c**,**g**,**i** are available online.

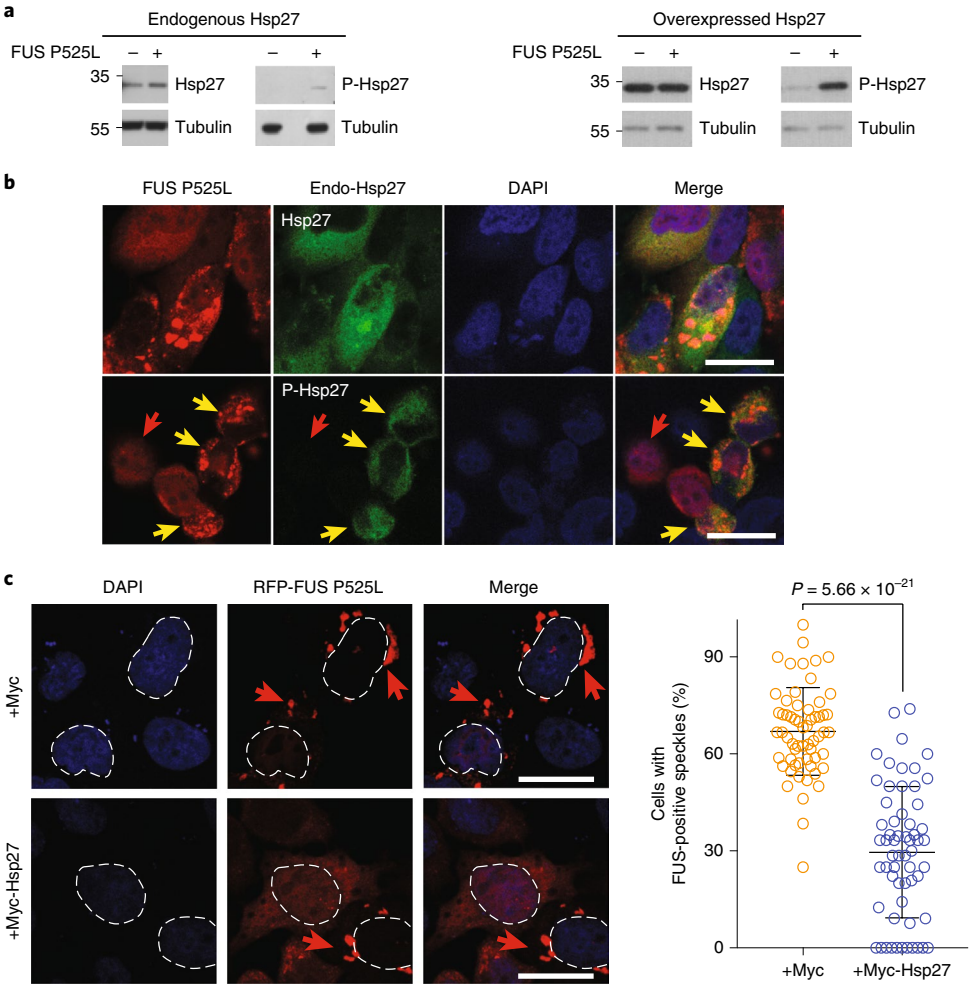

Fig. 6 | Phosphorylation of Hsp27 upon FUS P525L aggregation and mitigation of FUS aggregation in HeLa cells. a, Western blot of cell lysates expressing FUS P252L probed with antibodies for Hsp27 and phosphorylated Hsp27 (P-Hsp27, recognizing Ser82 phosphorylation). Endogenous (left) and overexpressed (right) Hsp27 are shown. Uncropped images are available as Source Data. **b**, Confocal images of HeLa cells transfected with RFP-FUS P525L (red) and stained with anti-Hsp27 (green, top row), anti-P-Hsp27 (green, bottom row) and DAPI (blue). The yellow arrows indicate cells with FUS aggregates that are stained with anti-P-Hsp27. The red arrows indicate cells without FUS aggregates. Scale bar, 20 μm. **c**, Confocal images of FUS P525L aggregation in the absence (top) or presence (bottom) of Myc-Hsp27 overexpression. Arrows indicate FUS aggregation. Scale bar, 20 μm. Right, graph showing statistics of 1,883 FUS-overexpressing cells from 120 images of four biologically independent samples. *P* value based on two-sided Student's *t* test. Source data for **c** are available online.

We further showed that Hsp27 can efficiently prevent the amyloid fibril formation of FUS LC using a ThT kinetic assay, confirmed using transmission electron microscopy (TEM) (Fig. 5h,i). Moreover, we observed that compared with the wild-type, Hsp27-3D exhibited enhanced activity to inhibit the amyloid aggregation of FUS LC (Fig. 5i). These data suggest that phosphorylation may weaken the inhibitory activity of Hsp27 in LLPS while enhancing its activity in amyloid aggregation.

Hsp27 is phosphorylated upon ALS-associated FUS P525L aggregation and mitigates the aggregation. It is known that Hsp27 is phosphorylated upon stress[41,42]. We found that the ALS-associated aggregation of FUS P525L formed in HeLa cells stressed the cells. FUS P525L is linked to a severe and juvenile form of ALS[43,44]. It mislocalizes to cytoplasm and forms LLPS-deficient big speckles[45–48]. To characterize the aggregation of FUS P525L, we applied pFTAA staining, which is a high-affinity, cell-permeant, β-sheet aggregation chemical probe[14]. The result showed that FUS P525L aggregates are specifically stained by pFTAA, which indicates the amyloid-like property of the aggregates (Extended Data Fig. 9a). Western blot on HeLa cells overexpressing FUS P525L showed that both the endogenous and exogenous Hsp27 proteins (at least part of them) are phosphorylated (Fig. 6a). Moreover, confocal microscopy showed that although Hsp27 exists in all cells, Hsp27 is phosphorylated only in the cells with FUS P525L aggregation (Fig. 6b). Upon Hsp27 overexpression and phosphorylation, we observed significant mitigation of the FUS P525L aggregation in cells (Fig. 6c), although the expression levels of FUS P525L remained unchanged (Extended Data Fig. 9b). Additionally, in the Hsp27-KO cells, FUS aggregation was observed upon stress (Fig. 1c). Taken together, these results indicate that abnormal FUS aggregation stresses the cells and induces the phosphorylation of Hsp27; conversely, phosphorylated Hsp27 reduces FUS aggregation, in line with the in vitro observation that phosphorylation (phosphomimics) increases Hsp27 activity in inhibiting amyloid aggregation.

Exposure of the ACD upon phosphorylation of Hsp27 causes enhanced amyloid inhibition. We next sought to understand why stress-induced phosphorylation can enhance the inhibition of Hsp27 on the amyloid aggregation of FUS LC. To dissect which

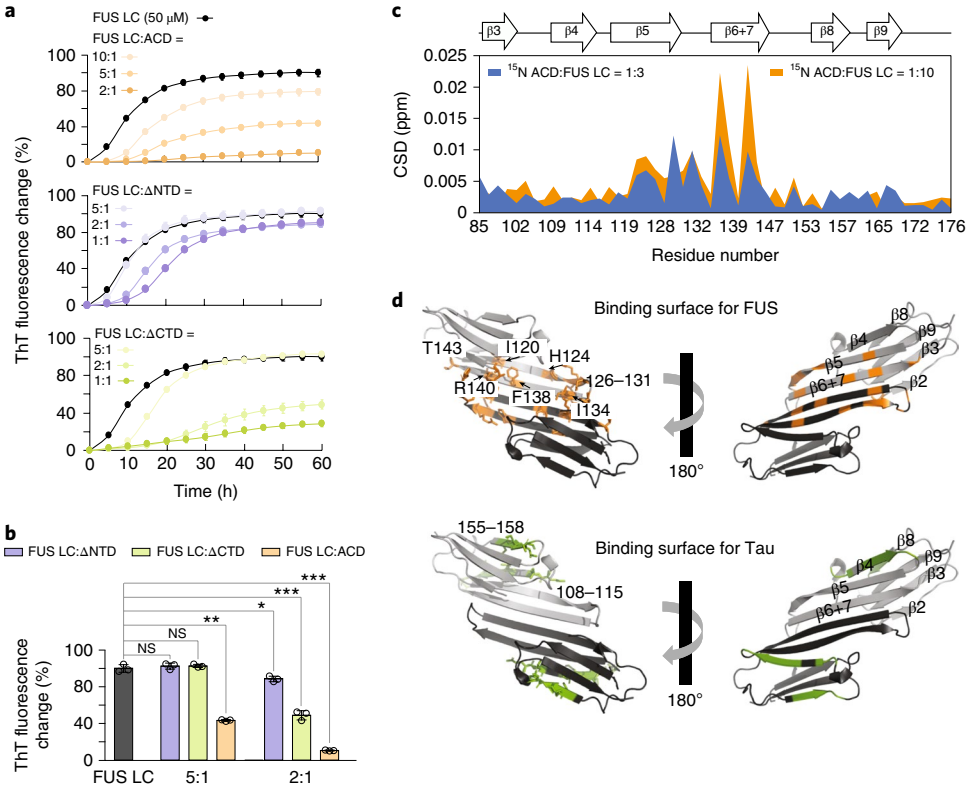

Fig. 7 | Molecular mechanism of Hsp27 inhibits FUS LC amyloid aggregation. a, ThT fluorescence profiles of FUS LC in the absence and presence of Hsp27 ACD (top), ΔNTD (middle), and ΔCTD (bottom) at the indicated concentrations. Data are plotted as mean ± s.d., with $n = 3$ biologically independent samples. **b**, Comparison of the inhibitory effect of Hsp27 variants on FUS LC amyloid aggregation. The ThT fluorescence intensities are taken at the 60-h time point in **a**. Data are plotted as mean ± s.d. with $n = 3$ biologically independent samples. $^*P < 0.05$, $^{**}P < 0.01$, $^{***}P < 0.001$. NS, not significant. *P* values based on two-sided Student's *t* test. **c**, Residue-specific chemical shift deviations of 150 μM Hsp27 ACD in the presence of 450 μM (blue) or 1.5 mM (orange) FUS LC. Secondary structural information for ACD is shown above. **d**, The binding surface of Hsp27 ACD for FUS (top) and Tau (bottom). Residues of Hsp27 ACD showing large chemical shift deviations (>0.005 ppm) upon FUS LC titration are highlighted in orange on the ribbon diagram of dimeric ACD (PDB 4MJH). The ACD binding surface for Tau is highlighted in green. Source data for graphs in **a**,**b** are available online.

domain is involved in the activity, we examined the activities of ACD, ΔNTD and ΔCTD. The results showed that truncation of either the NTD or the CTD moderately disrupted Hsp27 activity on the inhibition of FUS LC amyloid aggregation (Fig. 7a,b), which indicates that both terminal domains are important for activity. Notably, once both terminal domains were truncated, as seen with the ACD, the activity was largely restored by ~40% (Fig. 7a,b). This finding indicates that the activity of the ACD is screened by the NTD and the CTD. Given that Hsp27-3D exhibited a lower-order multimerization than that of the wild-type (Fig. 5d), the ACD might be more accessible in Hsp27-3D, which leads to an increased activity in the inhibition of amyloid aggregation. Together, our results indicate that in the inhibition of the amyloid aggregation of FUS LC, the activity of the ACD is screened by the NTD and the CTD. Stress-induced phosphorylation can release the ACD to some extent via demultimerization of Hsp27 and thus enhance the activity of Hsp27 in inhibiting FUS LC amyloid aggregation.

The Hsp27 ACD features distinct binding mechanisms for FUS and Tau. Because the ACD is the determinant for the amyloid inhibition of Hsp27, we explored the mechanism of the interaction between the Hsp27 ACD and FUS LC using NMR spectroscopy. The HSQC spectra showed that addition of FUS LC into ^{15}N-labeled Hsp27 ACD induced a moderate perturbation in chemical shift (>0.005 ppm) for residues, including V85, I120, H124, E126, R127, D129, H131, I134, F138, R140 and T143. These residues mainly cluster on the β5, β6 and β7 strands and the loops in between (Fig. 7c,d), forming a shallow cavity for FUS LC binding. To confirm the binding surface, we mutated these residues to alanine in full-length Hsp27, and we observed that the mutations markedly impaired the inhibitory activity of Hsp27 on the amyloid aggregation of FUS LC (Extended Data Fig. 10a,b).

A previous report on the interaction between Hsp27 ACD and Tau shows that the ACD binds to Tau with β4 and β8 (ref. [25]). Thus, the Hsp27 ACD utilizes different interfaces for the binding of FUS and Tau (Fig. 7d and Extended Data Fig. 10c). According to the previously reported structural model of Hsp27[26,32], although these two interfaces are both partially buried inside the Hsp27 multimers, the β5-β6-β7 interface is less accessible than the β4-β8 interface. Thus, ACD activity in amyloid inhibition might be more strictly regulated in the case of FUS.

Discussion

Although many RNA-binding proteins, such as FUS, hnRNPA1 and TDP43, can undergo a spontaneous and continuous process of LLPS and amyloid aggregation in vitro, their self-assembly and transition between different phases are tightly regulated in cells. In this study, we show a switchable activity of Hsp27, which precisely synchronizes with the phase transition of FUS. Our work suggests that Hsp27, which coexists with FUS in SGs, may serve as a key modulator to chaperone FUS in different phases under the fine regulation of phosphorylation in response to stress. It is known that Hsp27 is phosphorylated in response to various cellular stress including sodium arsenite, heat shock, oxidative stress and

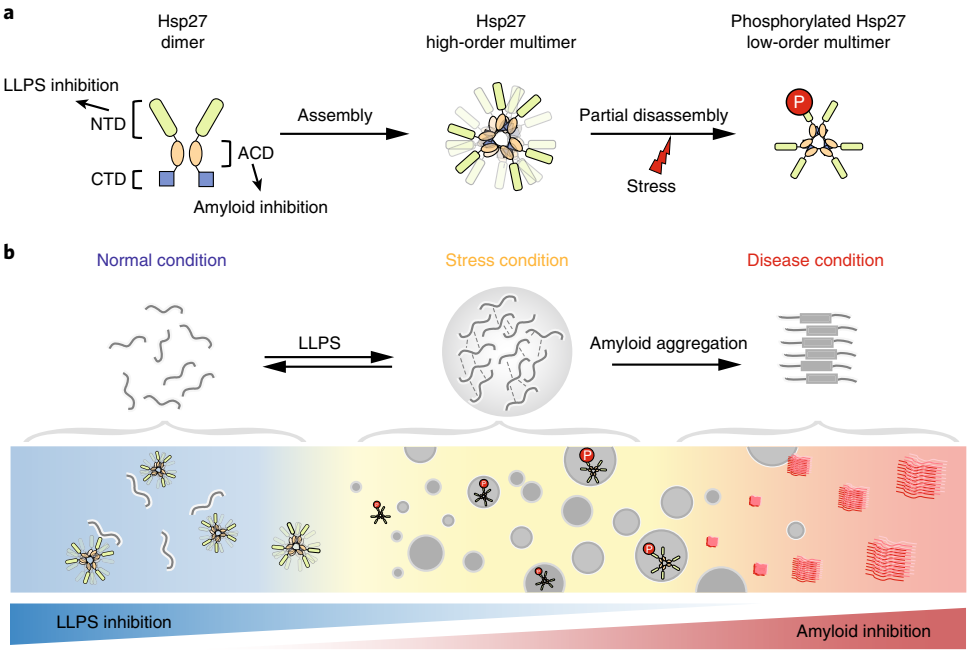

Fig. 8 | Schematic illustration of Hsp27 chaperoning FUS phase separation under the regulation of stress-induced post-translation phosphorylation. **a**, Hsp27 utilizes different domains for chaperoning FUS LLPS and amyloid aggregation. The multimeric assembly of Hsp27 is under the regulation of phosphorylation. Hsp27 domains are shown in different colors. Green, NTD; orange, ACD; purple, CTD. Under non-stress conditions, Hsp27 assembles into high-order multimers. In response to stress, Hsp27 is phosphorylated at the NTD and disperses. **b**, Under non-stress conditions, Hsp27 forms an ensemble of high-order multimers and inhibits phase separation of soluble FUS. Under stress conditions, FUS undergoes LLPS. At the same time, Hsp27 is phosphorylated and disassembles, which diminishes the inhibitory activity of Hsp27 on FUS LLPS while enhancing the ability of Hsp27 to inhibit FUS amyloid aggregation.

TNFα[41,42,49]. In this work, we found that FUS P525L aggregation can also stress the cells and induce Hsp27 phosphorylation. Mitogen-activated protein kinase (MAPK) signaling pathway and vascular endothelial growth factor signaling pathway have been reported to be involved in Hsp27 phosphorylation[42,50–52]. Both pathways lead to stimulation of the p38 MAPK cascade and subsequent activation of MAPK AP kinases 2 and 3, which phosphorylates Hsp27 (refs. [51,52]). In this work, we hypothesized that under normal conditions, Hsp27 is involved in safeguarding FUS in a soluble state. In response to stress, as FUS relocates from nuclei to SGs, Hsp27 is phosphorylated. The phosphorylated Hsp27 enters SGs to maintain the dynamic liquid-like state of FUS by preventing amyloid aggregation (Fig. 8). In addition to Hsp27, there are other chaperones that have been found to exist in SGs, such as Hsp90, Hsp70, Hsp40 and other small heat-shock proteins[16,17]. They may have different clients and roles and may coordinate to regulate the assembly and disassembly of SGs.

Hsp27 plays an important role in the cellular proteostasis network under both normal and stress conditions. Previous studies have revealed that Hsp27 features a high structural heterogeneity and conformational plasticity[24,26]. In aqueous solution, it exists as a collection of multimers with different sizes in an equilibrium of association and disassociation in an ATP-independent manner[24]. This structural flexibility enables Hsp27 to quickly adopt different conformations as tackling different client proteins upon environmental changes under energy-limiting conditions. In this work, we dissect the roles of the three domains of Hsp27. Our data show that the chaperone activity of Hsp27 to soluble FUS is mainly attributed to the NTD and the multimeric state. As for the chaperone activity of Hsp27 to phase-separated FUS, although all three domains are involved, the enhanced activity for amyloid inhibition is mainly derived from the exposure of the ACD upon phosphorylation on the NTD and the consequent de-multimerization (Fig. 8a). Thus, the structural plasticity enables Hsp27 to switch among different orders of self-assembly in response to different environment with different activities.

In the family of small heat-shock proteins, the ACD is conserved. The ACD from many small heat-shock proteins, such as αBc, have been reported to exhibit chaperone activity in inhibiting the aggregation of a variety of amyloid proteins and ameliorating toxicity in different disease-related models[25,33]. In contrast, the NTD is highly variable in terms of both sequence and length. Indeed, we show that αBc exhibits no activity in chaperoning FUS against LLPS, but it gains activity once the NTD is replaced by that of Hsp27. This finding implies that small heat-shock proteins may divergently evolve to chaperone different clients involved in different biological processes. For example, HspB8 is found to work with BAG3-Hsp70 to prevent the accumulation of defective ribosomal products in SGs[53]. Thus, small heat-shock proteins may play versatile yet important functions in the formation, maintenance and disassociation of various membraneless organelles.

Online content

Any methods, additional references, Nature Research reporting summaries, source data, extended data, supplementary information, acknowledgements, peer review information; details of author contributions and competing interests; and statements of data and code availability are available at https://doi.org/10.1038/s41594-020-0399-3.

Received: 27 June 2019; Accepted: 24 February 2020;
Published online: 30 March 2020

References

1. Banani, S. F., Lee, H. O., Hyman, A. A. & Rosen, M. K. Biomolecular condensates: organizers of cellular biochemistry. *Nat. Rev. Mol. Cell Biol.* **18**, 285–298 (2017).

2. Shin, Y. & Brangwynne, C. P. Liquid phase condensation in cell physiology and disease. *Science* **357**, eaaf4382 (2017).
3. Boeynaems, S. et al. Protein phase separation: a new phase in cell biology. *Trends Cell Biol.* **28**, 420–435 (2018).
4. Gui, X. et al. Structural basis for reversible amyloids of hnRNPA1 elucidates their role in stress granule assembly. *Nat. Commun.* **10**, 2006 (2019).
5. Patel, A. et al. A Liquid-to-solid phase transition of the ALS protein FUS accelerated by disease mutation. *Cell* **162**, 1066–1077 (2015).
6. Maharana, S. et al. RNA buffers the phase separation behavior of prion-like RNA binding proteins. *Science* **360**, 918–921 (2018).
7. Murakami, T. et al. ALS/FTD mutation-induced phase transition of FUS liquid droplets and reversible hydrogels into irreversible hydrogels impairs RNP granule function. *Neuron* **88**, 678–690 (2015).
8. Aguzzi, A. & Altmeyer, M. Phase separation: linking cellular compartmentalization to disease. *Trends Cell Biol.* **26**, 547–558 (2016).
9. Ramaswami, M., Taylor, J. P. & Parker, R. Altered ribostasis: RNA-protein granules in degenerative disorders. *Cell* **154**, 727–736 (2013).
10. Tyedmers, J., Mogk, A. & Bukau, B. Cellular strategies for controlling protein aggregation. *Nat. Rev. Mol. Cell Biol.* **11**, 777–788 (2010).
11. Hartl, F. U., Bracher, A. & Hayer-Hartl, M. Molecular chaperones in protein folding and proteostasis. *Nature* **475**, 324–332 (2011).
12. Guo, L. et al. Nuclear-import receptors reverse aberrant phase transitions of RNA-binding proteins with prion-like domains. *Cell* **173**, 677–692.e20 (2018).
13. Hofweber, M. et al. Phase separation of FUS is suppressed by its nuclear import receptor and arginine methylation. *Cell* **173**, 706–719.e13 (2018).
14. Qamar, S. et al. FUS phase separation is modulated by a molecular chaperone and methylation of arginine cation-π interactions. *Cell* **173**, 720–734.e15 (2018).
15. Yoshizawa, T. et al. Nuclear import receptor inhibits phase separation of FUS through binding to multiple sites. *Cell* **173**, 693–705.e22 (2018).
16. Jain, S. et al. ATPase-modulated stress granules contain a diverse proteome and substructure. *Cell* **164**, 487–498 (2016).
17. Mateju, D. et al. An aberrant phase transition of stress granules triggered by misfolded protein and prevented by chaperone function. *EMBO J.* **36**, 1669–1687 (2017).
18. Sharp, P. S. et al. Protective effects of heat shock protein 27 in a model of ALS occur in the early stages of disease progression. *Neurobiol. Dis.* **30**, 42–55 (2008).
19. Jesse, C. M. et al. ALS-associated endoplasmic reticulum proteins in denervated skeletal muscle: implications for motor neuron disease pathology. *Brain Pathol.* **27**, 781–794 (2017).
20. Dierick, I. et al. Genetic variant in the HSPB1 promoter region impairs the HSP27 stress response. *Hum. Mutat.* **28**, 830 (2007).
21. Benndorf, R., Martin, J. L., Kosakovsky Pond, S. L. & Wertheim, J. O. Neuropathy- and myopathy-associated mutations in human small heat shock proteins: characteristics and evolutionary history of the mutation sites. *Mutat. Res. Rev. Mutat. Res.* **761**, 15–30 (2014).
22. Bruey, J. M. et al. Hsp27 negatively regulates cell death by interacting with cytochrome c. *Nat. Cell Biol.* **2**, 645–652 (2000).
23. Choi, S., Chen, M., Cryns, V. L. & Anderson, R. A. A nuclear phosphoinositide kinase complex regulates p53. *Nat. Cell Biol.* **21**, 462–475 (2019).
24. Haslbeck, M., Franzmann, T., Weinfurtner, D. & Buchner, J. Some like it hot: the structure and function of small heat-shock proteins. *Nat. Struct. Mol. Biol.* **12**, 842–846 (2005).
25. Freilich, R. et al. Competing protein-protein interactions regulate binding of Hsp27 to its client protein tau. *Nat. Commun.* **9**, 4563 (2018).
26. van Montfort, R. L., Basha, E., Friedrich, K. L., Slingsby, C. & Vierling, E. Crystal structure and assembly of a eukaryotic small heat shock protein. *Nat. Struct. Biol.* **8**, 1025–1030 (2001).
27. Cox, D. et al. The small heat shock protein Hsp27 binds alpha-synuclein fibrils, preventing elongation and cytotoxicity. *J. Biol. Chem.* **293**, 4486–4497 (2018).
28. Yerbury, J. J. et al. The small heat shock proteins αB-crystallin and Hsp27 suppress SOD1 aggregation in vitro. *Cell Stress Chaperones* **18**, 251–257 (2013).
29. Baughman, H. E. R., Pham, T. T., Adams, C. S., Nath, A. & Klevit, R. E. Release of a disordered domain enhances HspB1 chaperone activity toward tau. *Proc. Natl Acad. Sci. USA* **117**, 2923–2929 (2020).
30. Jovcevski, B. et al. Phosphomimics destabilize Hsp27 oligomeric assemblies and enhance chaperone activity. *Chem. Biol.* **22**, 186–195 (2015).
31. Luo, F. et al. Atomic structures of FUS LC domain segments reveal bases for reversible amyloid fibril formation. *Nat. Struct. Mol. Biol.* **25**, 341–346 (2018).
32. Hochberg, G. K. et al. The structured core domain of αB-crystallin can prevent amyloid fibrillation and associated toxicity. *Proc. Natl Acad. Sci. USA* **111**, E1562–E1570 (2014).
33. Liu, Z. et al. Mechanistic insights into the switch of αB-crystallin chaperone activity and self-multimerization. *J. Biol. Chem.* **293**, 14880–14890 (2018).
34. Burke, K. A., Janke, A. M., Rhine, C. L. & Fawzi, N. L. Residue-by-residue view of in vitro FUS granules that bind the C-terminal domain of RNA polymerase II. *Mol. Cell* **60**, 231–241 (2015).
35. Dedmon, M. M., Lindorff-Larsen, K., Christodoulou, J., Vendruscolo, M. & Dobson, C. M. Mapping long-range interactions in α-synuclein using spin-label NMR and ensemble molecular dynamics simulations. *J. Am. Chem. Soc.* **127**, 476–477 (2005).
36. He, L., Sharpe, T., Mazur, A. & Hiller, S. A molecular mechanism of chaperone-client recognition. *Sci. Adv.* **2**, e1601625 (2016).
37. Bibow, S. et al. Structural impact of proline-directed pseudophosphorylation at AT8, AT100, and PHF1 epitopes on 441-residue tau. *J. Am. Chem. Soc.* **133**, 15842–15845 (2011).
38. Mainz, A. et al. The chaperone αB-crystallin uses different interfaces to capture an amorphous and an amyloid client. *Nat. Struct. Mol. Biol.* **22**, 898–905 (2015).
39. Pasta, S. Y., Raman, B., Ramakrishna, T. & Rao, Ch. M. The IXI/V motif in the C-terminal extension of alpha-crystallins: alternative interactions and oligomeric assemblies. *Mol. Vis.* **10**, 655–662 (2004).
40. Hayes, D., Napoli, V., Mazurkie, A., Stafford, W. F. & Graceffa, P. Phosphorylation dependence of Hsp27 multimeric size and molecular chaperone function. *J. Biol. Chem.* **284**, 18801–18807 (2009).
41. Landry, J. et al. Human HSP27 is phosphorylated at serines 78 and 82 by heat shock and mitogen-activated kinases that recognize the same amino acid motif as S6 kinase II. *J. Biol. Chem.* **267**, 794–803 (1992).
42. Rouse, J. et al. A novel kinase cascade triggered by stress and heat shock that stimulates MAPKAP kinase-2 and phosphorylation of the small heat shock proteins. *Cell* **78**, 1027–1037 (1994).
43. Chio, A. et al. Two Italian kindreds with familial amyotrophic lateral sclerosis due to FUS mutation. *Neurobiol. Aging* **30**, 1272–1275 (2009).
44. Conte, A. et al. P525L FUS mutation is consistently associated with a severe form of juvenile amyotrophic lateral sclerosis. *Neuromuscul. Disord.* **22**, 73–75 (2012).
45. Dormann, D. et al. ALS-associated fused in sarcoma (*FUS*) mutations disrupt Transportin-mediated nuclear import. *EMBO J.* **29**, 2841–2857 (2010).
46. Lo Bello, M. et al. ALS-related mutant FUS protein is mislocalized to cytoplasm and is recruited into stress granules of fibroblasts from asymptomatic FUS P525L mutation carriers. *Neurodegener. Dis.* **17**, 292–303 (2017).
47. Errichelli, L. et al. FUS affects circular RNA expression in murine embryonic stem cell-derived motor neurons. *Nat. Commun.* **8**, 14741 (2017).
48. De Santis, R. et al. Mutant FUS and ELAVL4 (HuD) aberrant crosstalk in amyotrophic lateral sclerosis. *Cell Reports* **27**, 3818–3831.e5 (2019).
49. Rogalla, T. et al. Regulation of Hsp27 oligomerization, chaperone function, and protective activity against oxidative stress/tumor necrosis factor α by phosphorylation. *J. Biol. Chem.* **274**, 18947–18956 (1999).
50. Stokoe, D., Engel, K., Campbell, D. G., Cohen, P. & Gaestel, M. Identification of MAPKAP kinase 2 as a major enzyme responsible for the phosphorylation of the small mammalian heat shock proteins. *FEBS Lett.* **313**, 307–313 (1992).
51. Ludwig, S. et al. 3pK, a novel mitogen-activated protein (MAP) kinase-activated protein kinase, is targeted by three MAP kinase pathways. *Mol. Cell. Biol.* **16**, 6687–6697 (1996).
52. Rousseau, S., Houle, F., Landry, J. & Huot, J. p38 MAP kinase activation by vascular endothelial growth factor mediates actin reorganization and cell migration in human endothelial cells. *Oncogene* **15**, 2169–2177 (1997).
53. Ganassi, M. et al. A surveillance function of the HSPB8-BAG3-HSP70 chaperone complex ensures stress granule integrity and dynamism. *Mol. Cell.* **63**, 796–810 (2016).

Methods

Plasmid construction. Genes of full-length human Hsp27 (UniProt accession number P04792), ACD (residues 85–176) and $N_{\alpha Bc}$-Hsp27 (αB crystallin, UniProt accession number P02511) were inserted into the pET-28a vector with an N-terminal His_6-tag and a TEV protease cleavage site. $Hsp27_{1-176}$ (ΔCTD), $Hsp27_{85-205}$ (ΔNTD) and N_{Hsp27}-αBc were cloned into the pET32a vector with an N-terminal PreScission protease-cleavable Trx1-tag and a His_6-tag. Hsp27-3D (S15/78/82D) and Hsp27-A (mutations of I120, H124, 126–131, I134, F136, R140 and T143 to alanine) were generated by site-directed mutagenesis of the wild-type vector using the Q5 Site-Directed Mutagenesis Kit (New England Biolabs). Myc-Hsp27 was constructed into a pCMV-Myc vector with an N-terminal Myc tag.

FUS was cloned with MBP fused at the N terminus with a PreScission protease cleavage site. FUS LC (residues 1–163) was cloned into a pHis-parallel vector (gifted from Dr. Chao Zhong at ShanghaiTech University). FUS LC S/A (mutated serine residues to alanine) was synthesized in the pHis-parallel vector. FUS RGG (residues 371–526) was constructed in a pET-28a vector with an N-terminal His_6-tag. RFP-FUS was cloned into pCAG. Sequences of all constructs were verified by GENEWIZ (Suzhou, China).

Protein expression and purification. All plasmids were expressed in *Escherichia coli* BL21 (DE3) cells. Cells were grown to an OD_{600} of 0.8 and induced with 0.5 mM IPTG overnight at 16 °C. Hsp27 and its variants were purified with a HisTrap FF column (GE Healthcare) with Tris buffer (50 mM Tris-HCl, 100 mM NaCl, a gradient of ~0–500 mM imidazole, pH 8.0). The N-terminal Trx1-tag was removed with PreScission protease in the buffer of 50 mM Tris-HCl, 100 mM NaCl, pH 8.0. The cleaved proteins were immediately loaded onto the size-exclusion chromatography column Superdex 75 26/60 (GE Healthcare). The PBS buffer was used for a Superdex 75 column containing 50 mM sodium phosphate, 50 mM NaCl, pH 7.0. All proteins were concentrated via centrifugal filtration (Amicon, Millipore) and flash frozen with liquid nitrogen.

FUS and FUS RGG were purified with a similar procedure as that for Hsp27, except that the buffer for the Superdex75 column contained 50 mM sodium phosphate and 500 mM NaCl, pH7.0. As for the purification of FUS LC and FUS LC S/A, cells were lysed by being suspended in 50 mM Tris-HCl, 100 mM NaCl, 6 M guanidinium hydrochloride at pH 8.0 and sonicated on ice. Cell supernatant was loaded on a HisTrap FF column (GE Healthcare) with Tris buffer (50 mM Tris-HCl, 100 mM NaCl, 6 M guanidinium hydrochloride with a gradient of ~0–500 mM imidazole, pH 8.0). The eluted protein was purified via high performance liquid chromatography (Agilent) and freeze dried by FreeZone lyophilizer (Thermo Fisher). The final storage buffer for purified FUS LC was 50 mM sodium phosphate, 50 mM NaCl, pH 7.0.

Proteins for NMR spectroscopy were expressed with *E. coli*, incubated in the M9 minimal medium with ^{15}N-labeled $NHCl_4$ (1 g/L) as the sole nitrogen source. Purification of ^{15}N-labeled proteins followed the same procedures as that for the unlabeled proteins.

Microscopic imaging for LLPS. We first labeled FUS LC with fluorescent dye. Proteins were incubated with ten-fold Oregon-Green 488 (Invitrogen, W6748) for 1 h, then run through a Superdex 75 26/60 size-exclusion chromatography column (GE Healthcare) in PBS buffer (50 mM sodium phosphate, 50 mM NaCl, pH 7.0). For fluorescence imaging, unlabeled FUS LC was mixed with labeled protein at the molar ratio of 49:1. Samples in PBS buffer (50 mM sodium phosphate, 50 mM NaCl, pH 7.0) were dropped on glass slides placed on a temperature-controlled stage (TP-CHSQ-C thermal stage) equipped with a Leica SP8 confocal microscopy. Images were taken with a DMI8 camera with a 100× objective (oil immersion).

Turbidity assay. LLPS of MBP FUS was initiated by diluting the NaCl concentration from 500 mM to 100 mM in 50 mM sodium phosphate, pH7.0. Absorbance at $OD_{600\,nm}$ was immediately measured with a Varioskan Flash spectral scanning multimode reader (Thermo Fisher Scientific) at room temperature.

LLPS of FUS LC, FUS LC S/A and FUS RGG occurred as the temperature decreased from 20 °C to 4 °C. Over the procedure, absorbance at $OD_{600\,nm}$ was measured with a Chirascan CD spectrometer (Applied Photophysics, UK). To test the activity of Hsp27 in reversing LLPS, both FUS LC and Hsp27 were cooled down to 4 °C before mixing. Absorbance was measured at 4 °C.

Protein overexpression in HeLa cells. HeLa cells were purchased from the Cell Bank of the Chinese Academy of Sciences, Shanghai (SCSP-504). The cell line was tested for mycoplasma contamination and has been authenticated. HeLa cells were grown in Dulbecco's modified medium (DMEM) supplemented with 10% fetal bovine serum (BioWest), 1% glutamine and 1% penicillin. Cells were grown to ~70% confluence for transfection. FUS and Hsp27 were transfected into cells using PolyJet (SignaGen Laboratories), for 6 h. After 24 h of recovery, 0.5 mM sodium arsenite was added into the medium for 1 h to induce the formation of SGs. Transfection and stress of Hsp27-KO cells was done with the same procedure as for the wild-type cells.

Hsp27 knockout in HeLa cells. Hsp27 was knocked out in HeLa cells using the CRISPR–Cas9 method. The target site for hHsp27 was designed as 'CTTGACCGT CAGCTCGTCCG' (for sgHsp27-2), and the GFP target site was 'GAGCTGGACGG CGACGTAAA' (for sgNC). As a negative control, oligos were synthesized and ligated into the LentiCRISPR V2-puro vector (Addgene plasmid # 52961) through standard protocol to generate sgHsp27 and sgNC. HEK293T cells were transfected with sgHsp27 or sgNC and pMD2.G (Addgene plasmid # 12259), psPAX (Addgene plasmid # 12260) at a ratio of 4:1:3. The virus-containing supernatant was harvested as described above and used to infect the cells. Twelve hours after infection, virus-infected HeLa cells were selected using puromycin (2 μg ml^{-1}) and validated.

Immunofluorescence imaging of HeLa cells by confocal microscopy. For imaging, cells were fixed with 4% paraformaldehyde in PBS for 15 min at room temperature. Fixed cells were washed three times with PBS and permeabilized for 10 min in 0.5% triton X-100, then blocked with 3% goat serum and 0.1% Triton X-100 in PBS for 1 h. Cells were incubated with anti-G3BP1 antibody (BD, Cat# 611127), anti-Hsp27 (Abcam, Cat# ab5579) or anti-phospho-Hsp27 (Cell Signaling Technology, Cat# 9709) overnight at 4 °C. AlexaFluor-488 and AlexaFluor-633 (Invitrogen) were used as the second antibodies. Coverslips were mounted with ProLong Gold Antifade Mountant with DAPI (Thermo Fisher, Cat# P36935). Images were acquired with a SP8 Leica microscope equipped with a DMI8 camera and analyzed with Leica AF Lite software. The percentage of FUS-positive SGs was calculated by the ratio of cells with FUS in SGs to the number of cells with transfected FUS.

For pFTAA staining, cells expressing CFP-FUS-P525L were grown on coverslips in a 24-well plate. After being fixed and permeabilized, cells were washed with PBS three times and incubated with 20 μM pFTAA, a high-affinity β-sheet aggregate chemical probe. Imaging was performed using an SP8 microscope with a 63× objective (water immersion). pFTAA was excited with a 514-nm laser. Each image was processed with Leica AF Lite software.

Western blot. Cell pellets were lysed with 1× loading buffer, then separated via sodium dodecyl sulfate (SDS) polyacrylamide gel electrophoresis and transferred to a PVDF membrane (Millipore). After being blocked with 5% skim milk for 1 h at room temperature, membranes were incubated with primary antibodies overnight, then secondary antibodies at room temperature. Primary antibodies were anti-Myc (Sigma, Cat# C3956), anti-Hsp27 (Abcam, Cat# ab5579), anti-phospho-Hsp27 (Cell Signaling Technology, Cat# 9709) and anti-alpha-crystallin (Abcam, Cat# ab76467).

Nuclear magnetic resonance spectroscopy. NMR experiments were done on a Bruker Avance 900 MHz spectrometer equipped with cryogenically cooled probes at 25 °C. ^{15}N-labeled FUS LC was prepared in PBS buffer (50 mM sodium phosphate, 50 mM NaCl, pH7.0) with 10% D_2O. Experimental sweep widths and assignments were based on a previous study[34]. The 2D ^{1}H-^{15}N HSQC spectra were recorded with 16 scans per transient and complex points of 2048 × 160. For titration experiments, we prepared 50 μM ^{15}N-FUS LC and indicated concentrations of Hsp27, both in PBS. For all titration experiments, each NMR sample (500 μl) was freshly made from high-concentration stock solutions. Intensity changes were calculated by I/I_0. And chemical shift deviations (CSD, Δδ) were calculated using the equation,

$$\Delta\delta = \sqrt{(\Delta\delta^{1}\mathrm{H})^{2} + 0.0289(\Delta\delta^{15}\mathrm{N})^{2}}$$

where $\Delta\delta^{1}H$ and $\Delta\delta^{15}N$ are the chemical shift differences of amide protons and amide nitrogens between the free and bound state of the protein, respectively.

The NMR spectrum of ^{15}N-labeled Hsp27 ACD was also acquired on the 900 MHZ NMR spectrometer. Backbone assignment was accomplished based on a previous study[54]. The operation and data collection were similar to that for ^{15}N-FUS LC.

MTSL labeling and paramagnetic relaxation enhancement experiments. Cysteine variants were cloned from wild-type FUS LC using a Q5 Site-Directed Mutagenesis Kit (New England Biolabs). ^{15}N-labeled or unlabeled proteins were prepared in 50 mM Tris-HCl, 100 mM NaCl, 8 M urea, pH 8.0. Dithiothreitol (DTT) was incubated with proteins at a molar ratio of 20:1 (DTT: protein) for 2 h. A HiPrep 26/10 Desalting column (GE Healthcare) was used to remove the DTT and then the proteins were mixed with MTSL (>10×) for 4 h at room temperature. Proteins were desalted into PBS buffer (50 mM sodium phosphate, 50 mM NaCl, pH 7.0) to remove excess MTSL. The proteins were then used for PRE experiments on a Bruker Avance 900 MHz at 298 K. To reduce the spin label, a final concentration of 1 mM ascorbate was added into the NMR tube. I_{param}/I_{diam} was calculated by measuring the resonance intensity of each residue of ^{15}N-FUS LC in the HSQC spectra without (I_{param}) and with (I_{diam}) ascorbate. We also attempted to obtain the PRE profiles of FUS LC by measuring Γ2 of the NMR samples. However, FUS LC quickly underwent LLPS beyond 100 μM at the NMR condition, and at concentrations lower than 100 μM, the NMR signal was too low to obtain the accurate Γ2 values using the traditional method[55]. Thus, we measured the I_{param}/I_{diam} of the samples as previously described[35,36,56].

Analytical ultracentrifugation. Sedimentation velocity experiments for various constructs of Hsp27 were performed at room temperature. All samples were operated on a Beckman Coulter xl-1 ultracentrifuge with an An60Ti eight-hole rotor (Beckman Instruments) at a speed of 30,000 r.p.m. Hsp27 variants, including Hsp27, Hsp27-3D, $N_{\alpha Bc}$-Hsp27, N_{Hsp27}-αBc, ΔCTD, ΔNTD and ACD, were

prepared at a final concentration of $OD_{280\,nm} = 0.6$ in PBS buffer (50 mM sodium phosphate, 50 mM NaCl, pH7.0). Absorbance data were collected at 280 nm in a continuous mode for at least 12 h. Data were analyzed with the program SEDFIT, with a continuous size-distribution (c(s)) model[57].

Liquid-like droplet maturation. For liquid-like droplet maturation, 100 μM CFP-labeled FUS LC was mixed with 10 μM Hsp27-3D in maturation buffer (50 mM sodium phosphate, 50 mM NaCl, pH7.0 and 20% dextran70). Fifteen microliters of the mixture was loaded onto the inner glass well of the dish (40 mm × 40 mm, 0.2 mm at thinnest bottom, NEST Biotechnology, Cat# 801001). A volume of 200 μl maturation buffer was loaded onto the outer plastic well of the dish to reduce volatilization. All the samples were incubated at room temperature for 20 h. Images were acquired with an SP8 Leica microscope with a 100× oil objective at indicated time points. Images were analyzed with Leica Application Suite X software.

Fluorescence recovery after photobleaching assay. For the FRAP assay, CFP-labeled FUS LC was mixed with or without Hsp27-3D at a molar ratio of 10:1. Preparation of samples was the same as that used in the maturation assay. The FRAP experiment was performed by using an SP8 Leica microscope with a 100× oil objective. A circular region approximately 2.5 μm in diameter was bleached for 2.5 s with full laser power. After being photobleached, images were acquired at 2.58 s per frame. For each time point, the fluorescence intensity was corrected by the intensity of a neighboring unbleached region.

Thioflavin T fluorescence assay. For the ThT assay, 50 μM of FUS LC in buffer containing 50 mM sodium phosphate, pH 7.0, 50 mM NaCl, 50 μM ThT and 0.05% NaN_3 was incubated with preformed fibril seeds (100:1) in clear 384-well plates (Costar). ThT fluorescence was monitored using a Varioskan Flash spectral scanning multimode reader (Thermo Fisher Scientific) with excitation at 440 nm and emission at 485 nm. Three replicates were performed for each sample.

FUS LC fibril seeds were prepared by incubating 200 mM FUS LC in buffer containing 50 mM Tris-HCl, 200 mM NaCl, pH 7.5, 0.05% NaN_3 at 25 °C for 6 days. Fibrils were sonicated into short fibril seeds.

Negative-staining transmission electron microscopy. Specimens of the ThT assay were verified with a Tecnai G2 Spirit transmission electron microscope operated at an accelerating voltage of 120 kV. Eight-microliter samples were transferred to carbon-coated grids for 1 min and stained with 8 μl uranyl acetate (2% v/v) for 45 s. Images were acquired using a 4,000 × 4,000 charge-coupled device camera (BM-Eagle, FEI Tecnai).

Reporting Summary. Further information on research design is available in the Nature Research Reporting Summary linked to this article.

Data Availability Statement

Source data for Fig. 1a,b, 2c, 4b,g, 5c,g,i, 6a,c and 7a,b are available with the paper online.

References

54. Rajagopal, P., Liu, Y., Shi, L., Clouser, A. F. & Klevit, R. E. Structure of the α-crystallin domain from the redox-sensitive chaperone, HSPB1. *J. Biomol. NMR* **63**, 223–228 (2015).
55. Fawzi, N. L., Ying, J., Torchia, D. A. & Clore, G. M. Kinetics of amyloid β monomer-to-oligomer exchange by NMR relaxation. *J. Am. Chem. Soc.* **132**, 9948–9951 (2010).
56. Oroz, J. et al. Structure and pro-toxic mechanism of the human Hsp90/PPIase/Tau complex. *Nat. Commun.* **9**, 4532 (2018).
57. Peschek, J. et al. Regulated structural transitions unleash the chaperone activity of αB-crystallin. *Proc. Natl Acad. Sci. USA* **110**, E3780–E3789 (2013).

Acknowledgements

We thank staff members of the National Center for Protein Science Shanghai for assistance in NMR data collection. This work was supported by the National Natural Science Foundation (NSF) of China (91853113 to D.L. and C.L.), the Major State Basic Research Development Program (2016YFA0501902 to C.L.), the Science and Technology Commission of Shanghai Municipality (18JC1420500 to C.L.), Shanghai Pujiang Program (18PJ1404300 to D.L.), the "Eastern Scholar" project supported by Shanghai Municipal Education Commission (to D.L.), Shanghai Municipal Science and Technology Major Project (2019SHZDZX02 to C.L.), and Innovation Program of Shanghai Municipal Education Commission (2019-01-07-00-02-E00037 to D.L.).

Author contributions

D.L., C.L. and Zhenying Liu designed the project. Zhenying Liu, Yichen Li, J.L., H.L. and X.G. prepared constructs and purified proteins. Zhenying Liu, J.G., Ying Li and Y.T. performed the biochemical and cellular assays. Zhenying Liu, S.Z., C.W., C.Z. and Zhijun Liu performed the NMR experiments. D.L. wrote the manuscript. D.L., C.L., and L.H. revised the manuscript.

Competing interests

The authors declare no competing interests.

Additional information

Extended data is available for this paper at https://doi.org/10.1038/s41594-020-0399-3.

Supplementary information is available for this paper at https://doi.org/10.1038/s41594-020-0399-3.

Correspondence and requests for materials should be addressed to D.L. or C.L.

Peer review information Anke Sparmann was the primary editor on this article and managed its editorial process and peer review in collaboration with the rest of the editorial team.

Reprints and permissions information is available at www.nature.com/reprints.

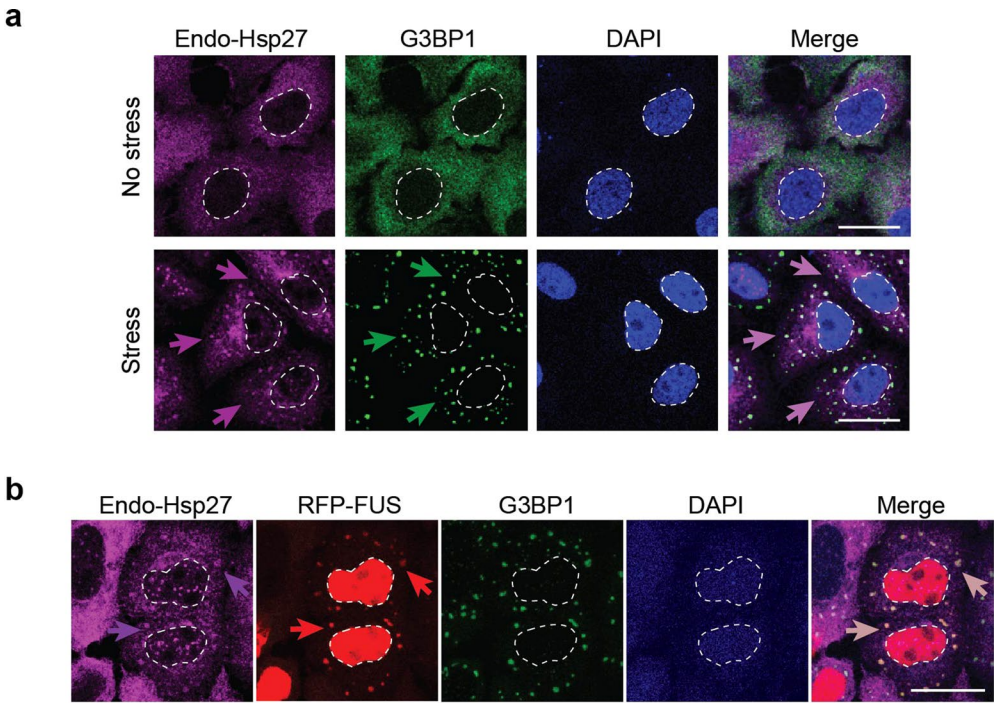

Extended Data Fig. 1 | Intracellular localization of endogenous Hsp27. a, Endogenous Hsp27 (endo-Hsp27, red) of HeLa cells localizes in the cytoplasm under normal condition. As treated with stress (0.5 mM sodium arsenite), endo-Hsp27 condenses in SGs. Cells were immunostained for DAPI (blue). Scale bar, 20 μm. **b**, HeLa cells expressing RFP-FUS were treated with stress (0.5 mM sodium arsenite). Co-localization of Hsp27 (purple) and overexpressed RFP FUS (red) in SGs are indicated with arrows. Cells were immunostained for G3BP1 (green) to mark SGs. Scale bar, 20 μm.

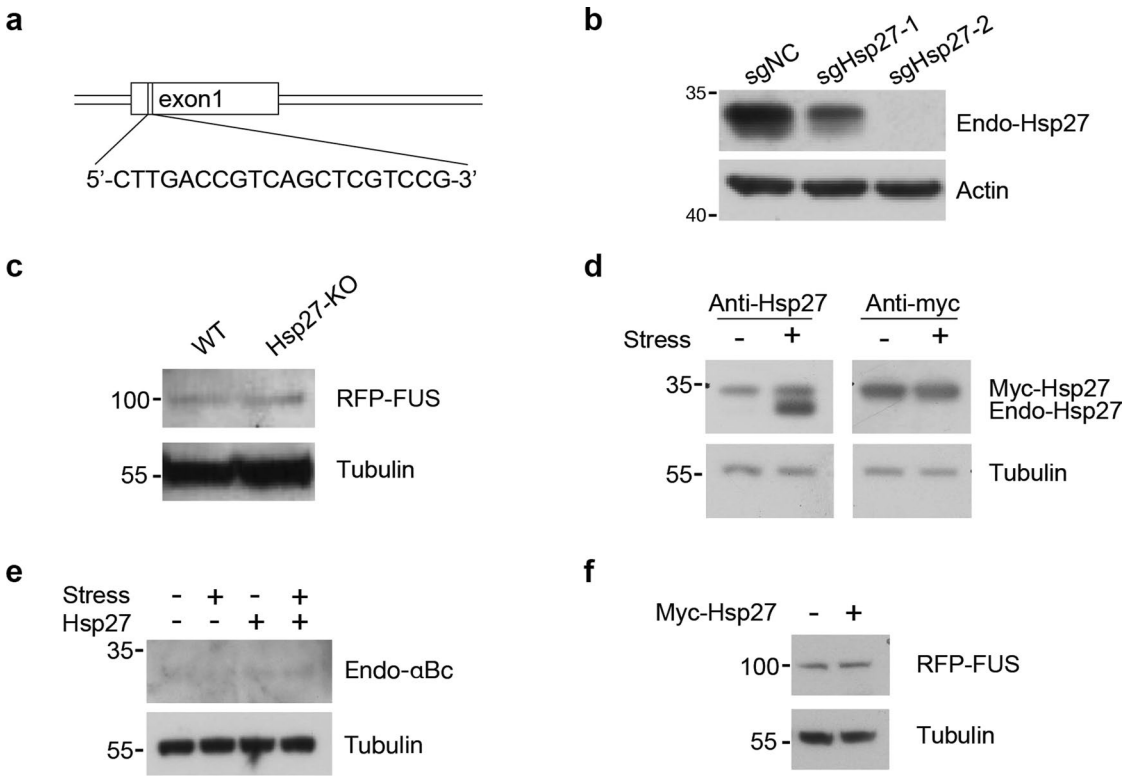

Extended Data Fig. 2 | Establishment of Hsp27 KO HeLa cells and cellular expression levels of FUS, Hsp27 and αBc (control) by western blot. a, A fragment in Hsp27 exon 1 was deleted by using CRISPR/Cas9. We constructed two KO plasmids—sgHsp27-1 and sgHsp27-2. **b**, Western blot shows that plasmid sgHsp27-2 is efficient to suppress Hsp27 expression. sgNC is empty plasmid transfected in cells as control. **c**, A similar expression level of FUS in the Hsp27 KO and WT cells. **d**, Expression of endogenous (endo-Hsp27) and exogenous (myc-Hsp27) with/without stress (0.5 mM sodium arsenite). **e**, Expression levels of αBc with or without stress and Hsp27 overexpression. **f**, A similar expression level of FUS in cells with or without myc-Hsp27 overexpression.

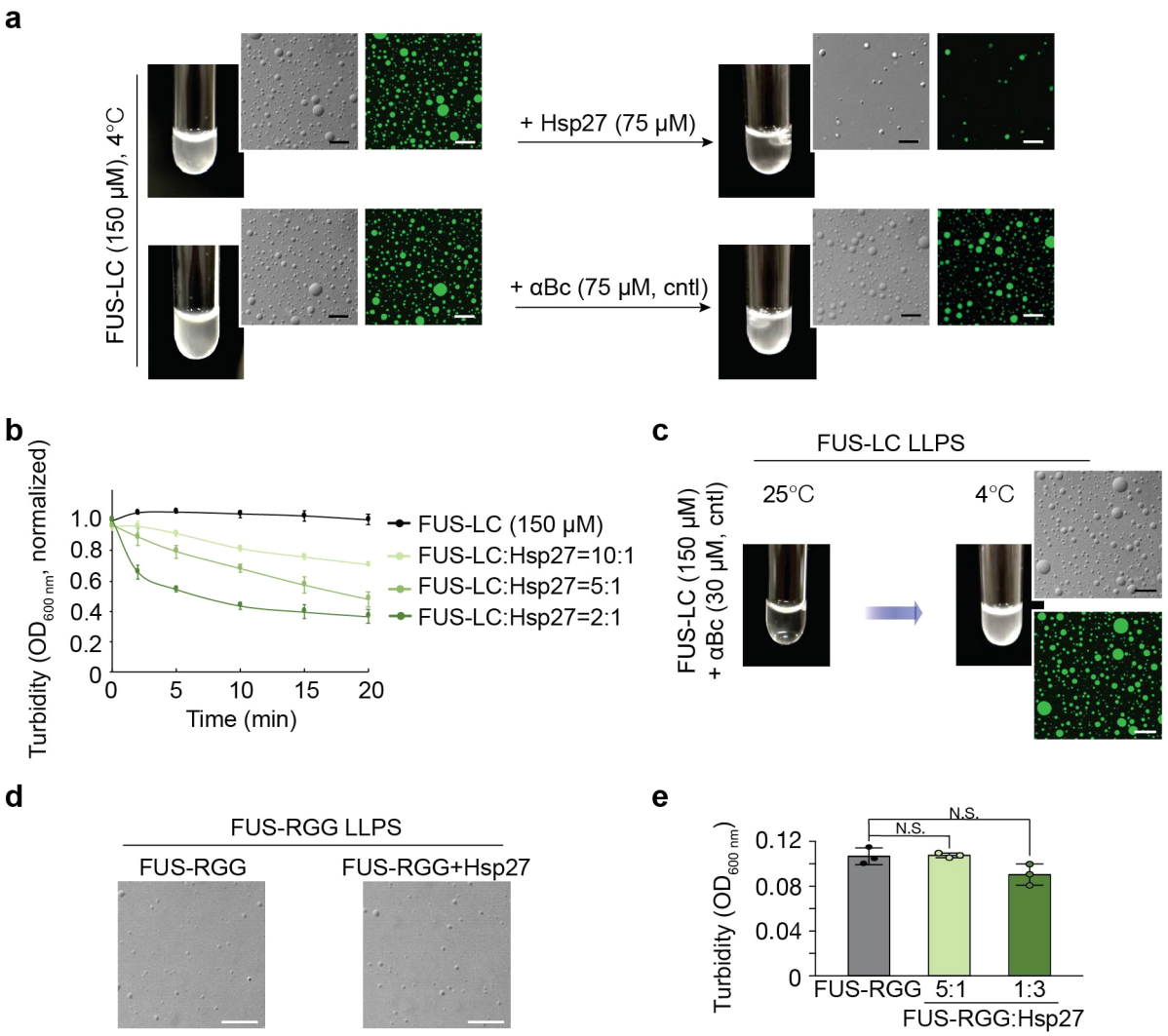

Extended Data Fig. 3 | Hsp27 reverses the LLPS of FUS-LC, while exhibits no effect on FUS-RGG LLPS. a, Visualization of the reversion of Hsp27 to FUS-LC LLPS in test tubes and by DIC and fluorescence imaging. Scale bar: 10 μm. αBc is performed as a negative control. **b**, The LLPS of 150 μM FUS-LC was induced by decreasing the temperature to 4 °C, followed by the measurement of turbidities at $OD_{600\,nm}$. The molar ratios of Hsp27 are indicated. Error bars correspond to mean ± S.D. with n=3. **c**, αBc (negative control) exhibits no effect on FUS-LC LLPS. The test tubes contain 150 μM FUS-LC in the presence of 30 μM αBc at 25 °C and 4 °C, respectively. The DIC and fluorescence images show the liquid-like droplets formed by FUS-LC. Scale bar: 10 μm. **d**, Effect of Hsp27 on the LLPS of FUS-RGG. DIC images are shown with scale bars representing 10 μm. **e**, Turbidity measurement of 50 μM FUS-RGG in the presence of indicated ratios of Hsp27 at 4 °C. Error bars correspond to mean ± S.D., with n = 3. N. S. indicates not significant.

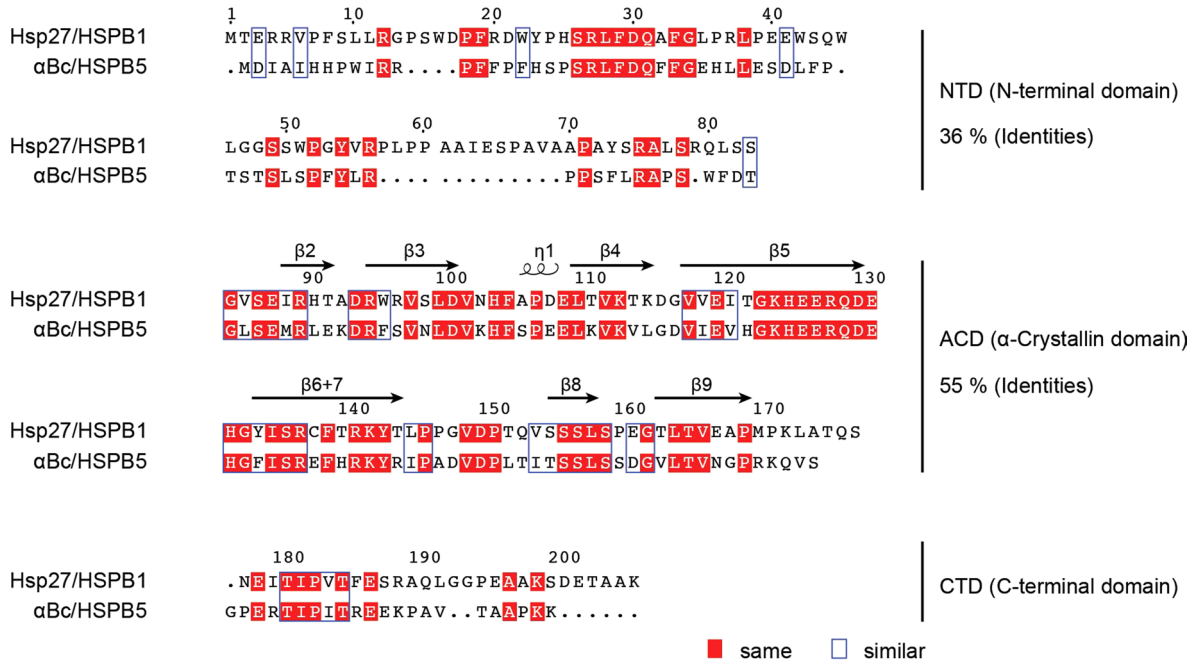

Extended Data Fig. 4 | Sequence alignment of Hsp27 (HSPB1) and αBc (HSPB5). The alignment was performed by software ClustalX and ESPript 3.0. The identities of NTDs and ACDs are labeled, respectively. The CTDs vary with no significant identity.

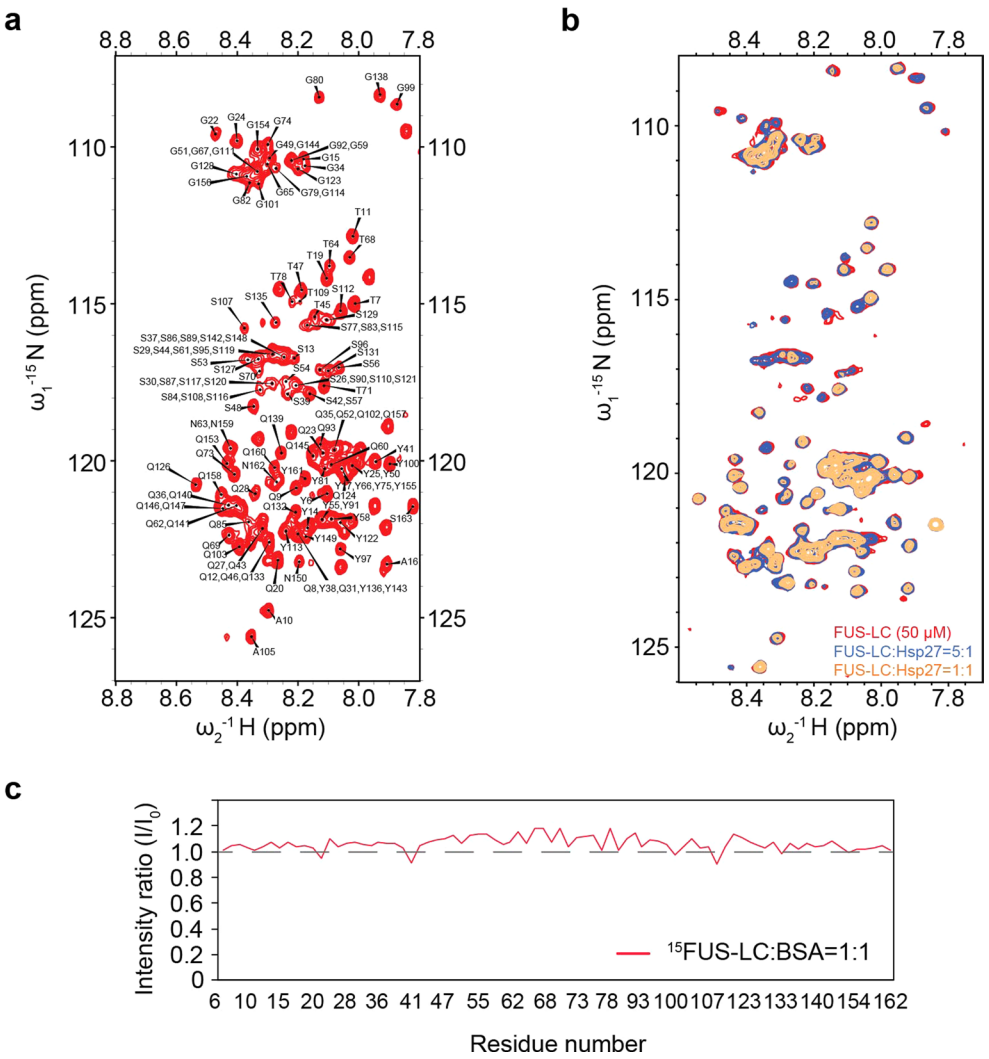

Extended Data Fig. 5 | NMR spectra of FUS-LC titrated with Hsp27. a, The backbone assignment of FUS-LC (50 μM) with resonances labeled by one amino acid letter and the residue number in FUS. **b**, Overlay of the 2D ^{1}H-^{15}N HSQC spectra of 50 μM ^{15}N-FUS-LC alone (red) and in the presence of Hsp27 at molar ratios (FUS-LC: Hsp27) of 5:1 (blue) and 1:1 (orange), respectively. **c**, Residue-specific intensity changes of 50 μM FUS-LC in the presence of 50 μM BSA (red) as a negative control. The dash line indicates the line of I/I$_0$=1.0.

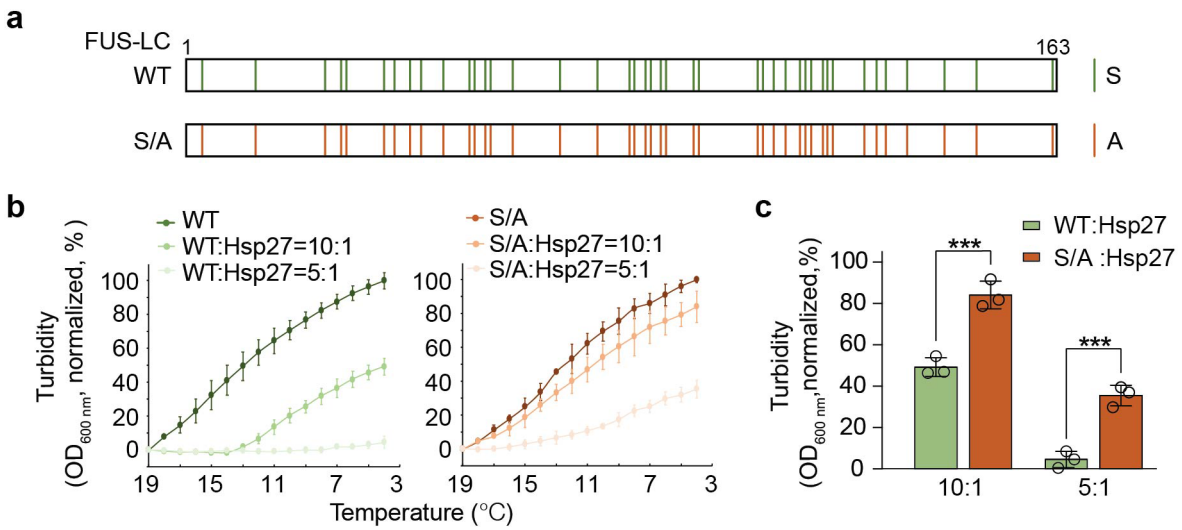

Extended Data Fig. 6 | Mutation of the Ser residues of FUS-LC impairs the inhibition of Hsp27 to FUS-LC LLPS. a, Schematics show the Ser residues (green) of FUS-LC that are mutated into Ala (red). The mutation construct is named S/A. **b**, Turbidity measurements of FUS-LC WT (left) and S/A (right) in the presence of Hsp27. **c**, Comparison of the effect of Hsp27 on the LLPS of FUS LC-WT and S/A. The turbidity values are those in (b) at 4 °C. Data shown correspond to mean ± S.D., n = 3. *** $p<0.001$ by Student's t-test.

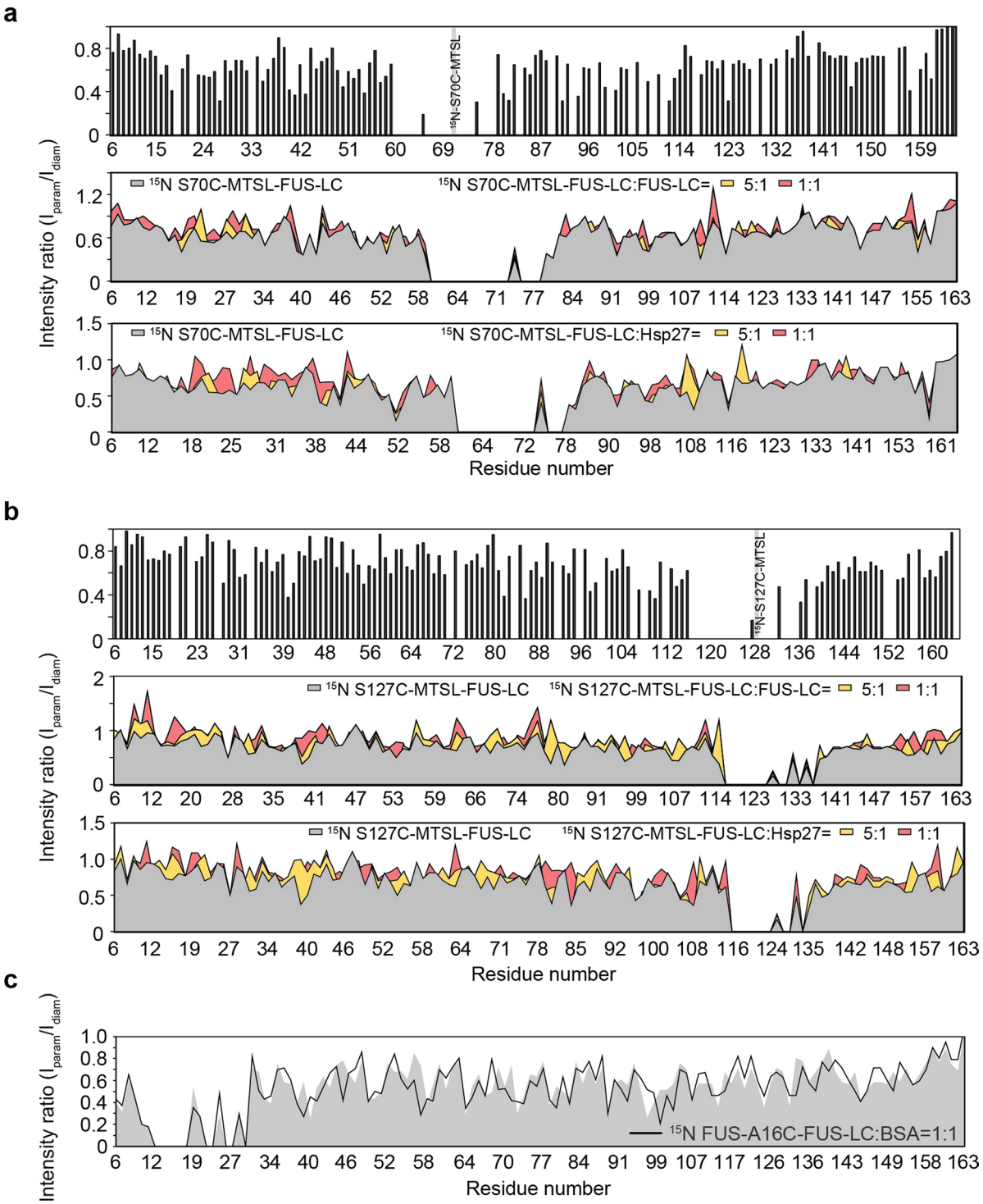

Extended Data Fig. 7 | Effect of Hsp27 on the long-range and transient interactions of FUS-LC probed by PRE. a, The PRE profile of 50 μM ^{15}N S70C-MTSL-FUS-LC is shown on the top. The PRE attenuations were recovered with increasing concentrations of 10 μM (orange) and 50 μM (red) unlabeled FUS-LC is shown in the middle, and with 10 μM (orange) and 50 μM (red) Hsp27 is shown at the bottom. **b**, The PRE profiles of 50 μM ^{15}N S127C-MTSL-FUS-LC. **c**, The effect of BSA (50 μM, negative control) on 50 μM ^{15}N A16C-MTSL-FUS-LC.

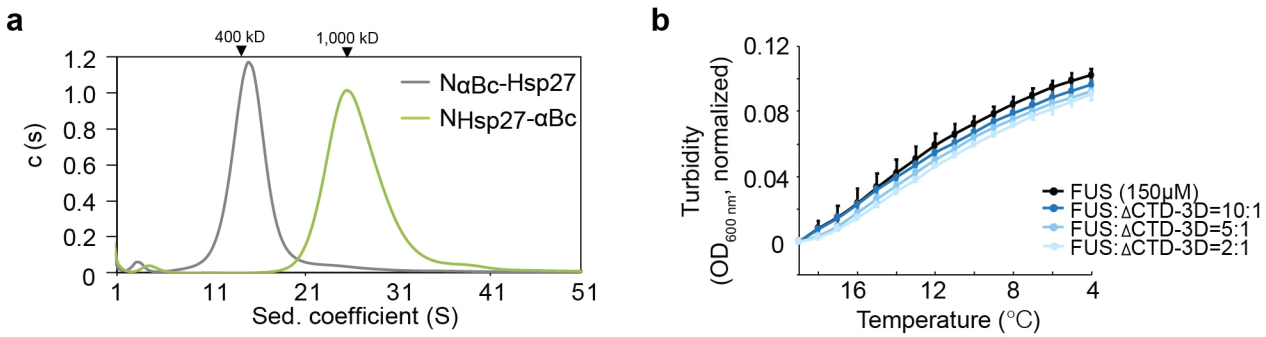

Extended Data Fig. 8 | Sedimentation velocity analysis of $N_{\alpha Bc}$-Hsp27 and N_{Hsp27}-αBc, and the influence of Hsp27 ΔCTD-3D on FUS-LC LLPS. **a**, Sedimentation velocity analysis of $N_{\alpha Bc}$-Hsp27 (20 μM) and N_{Hsp27}-αBc (17 μM). **b**, The influence of Hsp27 ΔCTD-3D on the phase transition of FUS-LC. The turbidity ($OD_{600\ nm}$) of 150 μM FUS-LC in the absence and presence of ΔCTD-3D at the indicated concentrations were monitored from 19 °C to 4 °C.

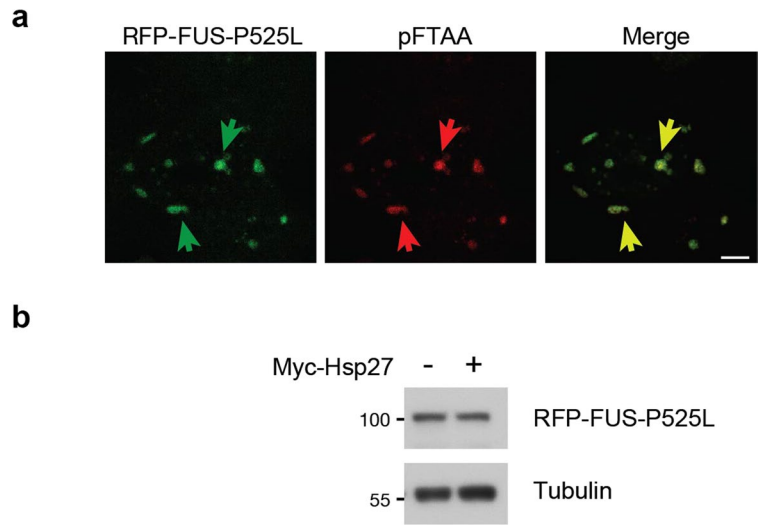

Extended Data Fig. 9 | Characterization of FUS P525L expression and aggregation in HeLa cells. a, Confocal microscopic images show the pFTAA staining of FUS P525L aggregates in HeLa cells. FUS P525L was overexpressed and spontaneously aggregated in cells. **b**, Western blot showed that the expression level of FUS P525L remains unchanged with/without the overexpression of myc-Hsp27.

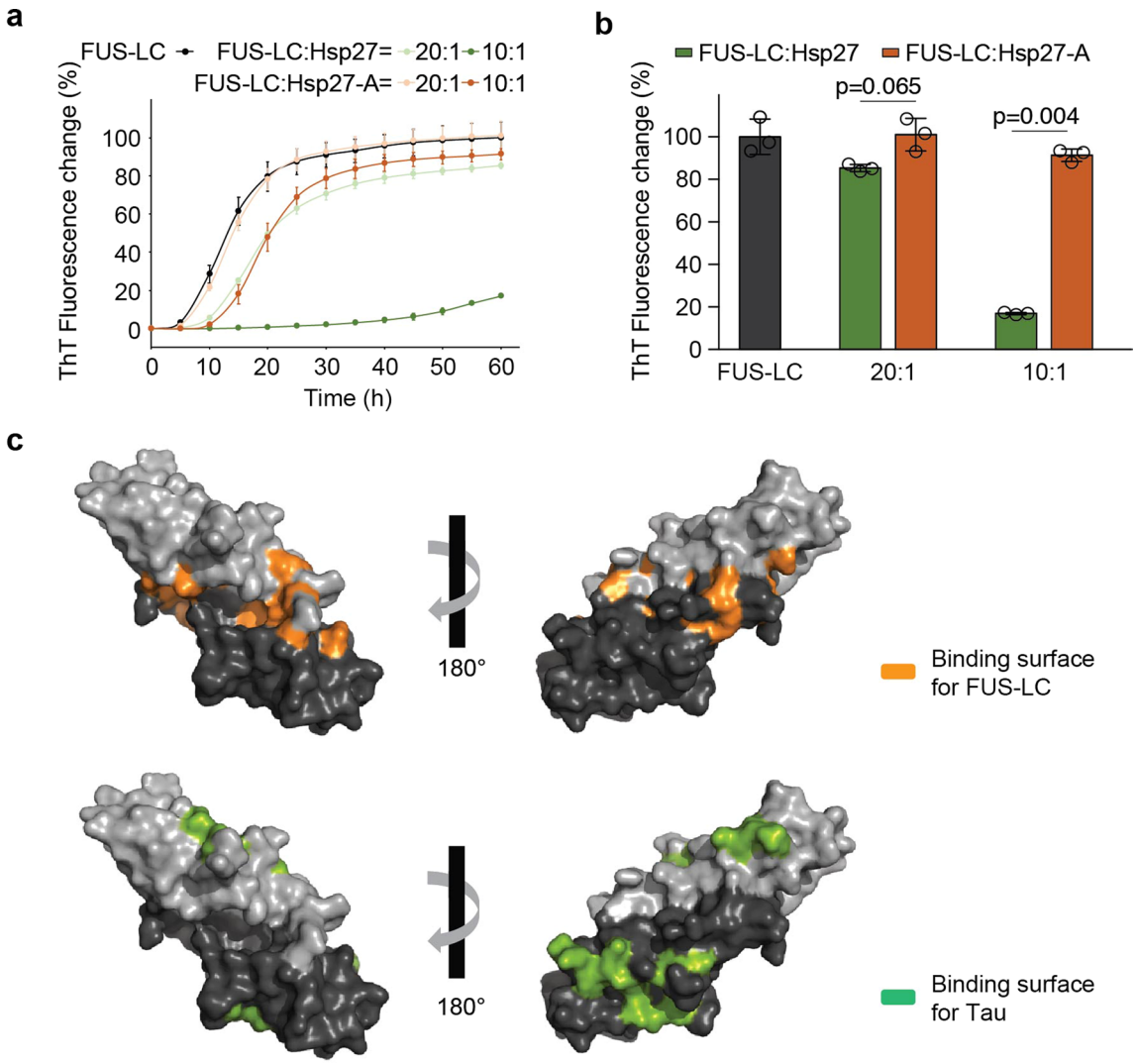

Extended Data Fig. 10 | Mutagenesis of the binding surface of Hsp27 with FUS-LC impaired the inhibitory activity of Hsp27 to FUS-LC amyloid aggregation. a, ThT fluorescence assay shows that the mutated Hsp27 (Hsp27-A) exhibits decreased inhibitory activity to FUS-LC amyloid aggregation, compared to the WT Hsp27. **b**, Statistics of data in (**a**) at 60 h. Data shown are mean ± S.D., n = 3. **c**, Surface representation of the structure of Hsp27 ACD dimer. Binding interface of Hsp27 ACD for FUS-LC (upper) is highlighted in orange on the surface diagram of ACD (PDB code, 4MJH); that for Tau (lower) is highlighted in green.

nature research

Corresponding author(s): Dan Li, Cong Liu

Last updated by author(s): Feb 17, 2020

Reporting Summary

Nature Research wishes to improve the reproducibility of the work that we publish. This form provides structure for consistency and transparency in reporting. For further information on Nature Research policies, see Authors & Referees and the Editorial Policy Checklist.

Statistics

For all statistical analyses, confirm that the following items are present in the figure legend, table legend, main text, or Methods section.

n/a	Confirmed	
☐	☒	The exact sample size (*n*) for each experimental group/condition, given as a discrete number and unit of measurement
☐	☒	A statement on whether measurements were taken from distinct samples or whether the same sample was measured repeatedly
☐	☒	The statistical test(s) used AND whether they are one- or two-sided *Only common tests should be described solely by name; describe more complex techniques in the Methods section.*
☒	☐	A description of all covariates tested
☒	☐	A description of any assumptions or corrections, such as tests of normality and adjustment for multiple comparisons
☐	☒	A full description of the statistical parameters including central tendency (e.g. means) or other basic estimates (e.g. regression coefficient) AND variation (e.g. standard deviation) or associated estimates of uncertainty (e.g. confidence intervals)
☐	☒	For null hypothesis testing, the test statistic (e.g. *F*, *t*, *r*) with confidence intervals, effect sizes, degrees of freedom and *P* value noted *Give P values as exact values whenever suitable.*
☒	☐	For Bayesian analysis, information on the choice of priors and Markov chain Monte Carlo settings
☒	☐	For hierarchical and complex designs, identification of the appropriate level for tests and full reporting of outcomes
☒	☐	Estimates of effect sizes (e.g. Cohen's *d*, Pearson's *r*), indicating how they were calculated

Our web collection on statistics for biologists contains articles on many of the points above.

Software and code

Policy information about availability of computer code

Data collection	We used LAS X (Leica) for confocal collection.
Data analysis	We used Image J for image analysis. Structure model were processed by Pymol. Sparky, NMRViewJ and nmrPipe were used to analyze the NMR data.

For manuscripts utilizing custom algorithms or software that are central to the research but not yet described in published literature, software must be made available to editors/reviewers. We strongly encourage code deposition in a community repository (e.g. GitHub). See the Nature Research guidelines for submitting code & software for further information.

Data

Policy information about availability of data

All manuscripts must include a data availability statement. This statement should provide the following information, where applicable:

- Accession codes, unique identifiers, or web links for publicly available datasets
- A list of figures that have associated raw data
- A description of any restrictions on data availability

The data of this study are available from the corresponding author upon request. Source data for Figs 1, 2, 4 and 6 are available with the paper online.

Field-specific reporting

Please select the one below that is the best fit for your research. If you are not sure, read the appropriate sections before making your selection.

☒ Life sciences ☐ Behavioural & social sciences ☐ Ecological, evolutionary & environmental sciences

For a reference copy of the document with all sections, see nature.com/documents/nr-reporting-summary-flat.pdf

Life sciences study design

All studies must disclose on these points even when the disclosure is negative.

Sample size	The experiments described in this study were performed with more than 3 samples for each group.
Data exclusions	None
Replication	At least three independent biological repeats were performed.
Randomization	None
Blinding	None

Reporting for specific materials, systems and methods

We require information from authors about some types of materials, experimental systems and methods used in many studies. Here, indicate whether each material, system or method listed is relevant to your study. If you are not sure if a list item applies to your research, read the appropriate section before selecting a response.

Materials & experimental systems

n/a	Involved in the study
☐	☒ Antibodies
☐	☒ Eukaryotic cell lines
☒	☐ Palaeontology
☒	☐ Animals and other organisms
☒	☐ Human research participants
☒	☐ Clinical data

Methods

n/a	Involved in the study
☒	☐ ChIP-seq
☒	☐ Flow cytometry
☒	☐ MRI-based neuroimaging

Antibodies

Antibodies used	anti-G3BP1 (BD, Cat. Lot: 611127); anti-Hsp27 (abcam, Cat. Lot: ab5579); anti-phospho-Hsp27 (Cell signaling, Cat. Lot: 9709); anti-myc (sigma, Cat. Lot: C3956); anti-alpha-crystallin (abcam, Cat. Lot: ab76467) Goat anti-Rabbit IgG (H+L), Secondary Antibody, Alexa Fluor 633 (ThermoFisher, Cat. Lot: A-21071) Goat anti-Mouse IgG (H+L), Secondary Antibody, Alexa Fluor 488 (ThermoFisher, Cat. Lot: A-11001)
Validation	The antibodies are well validated for the indicated use by the manufacturer available on their websites.

Eukaryotic cell lines

Policy information about cell lines

Cell line source(s)	Hela cells were purchased from cell Bank of the Chinese Academy of Sciences, Shanghai.
Authentication	Hela cells have been authenticated by STR method.
Mycoplasma contamination	The cell line is negative for mycoplasma contamination.
Commonly misidentified lines (See ICLAC register)	No commonly misidentified cell lines were used.